

# The energetics of stalk intermediates in membrane fusion are controlled by lipid composition

## – SI Appendix –

Sebastian Aefferer\*   Tobias Reusch\*   Britta Weinhausen\*   Tim Salditt\*<sup>†</sup>

March 4, 2012

## 1 Sample preparation

Solid-supported, oriented lipid bilayer stacks were prepared by deposition from organic solution based on the protocol introduced by Seul and Sammon [1]. To this end, polished silicon wafers cut to substrates of  $15 \times 10 \text{ mm}^2$  and  $25 \times 15 \text{ mm}^2$  were purchased from Silchem (Freiberg, Germany). The lipids 1,2-dioleoyl-*sn*-glycero-3-phosphocholine (di18:1( $\Delta 9$ -*cis*)PC, DOPC), 1,2-dipalmitoleoyl-*sn*-glycero-3-phosphocholine (di16:1( $\Delta 9$ -*cis*)PC), 1,2-dimyristoleoyl-*sn*-glycero-3-phosphocholine (di14:1( $\Delta 9$ -*cis*)PC), 1,2-diphytanoyl-*sn*-glycero-3-phosphocholine (4ME 16:0 PC, DPhPC), 1,2-dioleoyl-*sn*-glycero-3-phosphoethanolamine (di18:1( $\Delta 9$ -*cis*)PE, DOPE) and cholesterol (Chol) were purchased as lyophilized powders from Avanti Polar Lipids (Alabaster, AL, USA) and used as delivered. The substrates were thoroughly cleaned by repeated washing cycles with methanol and deionized water in an ultrasonic bath, dried in a nitrogen stream, rendered hydrophilic in a plasma cleaner and placed on a horizontally aligned table. Lipid stock solutions were prepared in chloroform/(2,2,2)-trifluoroethanol (1:1 vol:vol) with a concentration of 10 mg/ml. For DOPC/DOPE and DOPC/Chol mixtures, stock solutions were combined in the required ratios and thoroughly vortexed. 80  $\mu\text{l}$  lipid solution were then pipetted uniformly onto the  $15 \times 10 \text{ mm}^2$  substrates, for the larger substrates the volume was increased to 200  $\mu\text{l}$ . After few hours, the bulk solvent had evaporated and the lipids formed a stable thin film. Residual solvent was extracted by storage in vacuum for at least 12 h. For an area per lipid headgroup of about  $70 \text{ \AA}^2$  [2], the number of bilayers in a stack is approximately 1400 for both substrate sizes.

For powder measurements, lipid solutions of considerably higher concentrations of 0.5 or 1 g/ml were prepared in order to achieve sufficiently high scattering volumes. For each sample, 10  $\mu\text{l}$  were pipetted onto an area of approximately  $10 \times 2 \text{ mm}^2$  on a cellulose/polyester wiper (Dux 670, Berkshire). Solvent extraction was achieved in the same way as for the oriented samples. The sheet was then cut into several stripes about 2 mm in width. These were stacked on top of each other in order to maximize the amount of lipid accessible for the x-ray beam (Fig. S3a).

## 2 Hydration control and lipid polymorphism

Between sample preparation and experiments, samples were stored at  $T = 7^\circ\text{C}$ . Prior to data collection, they were rehydrated and brought to room temperature in an atmosphere saturated with water vapour. Subsequently, they were placed in environmental chambers equipped with polypropylene or Kapton windows for the passage of x-rays. These were connected to a setup for relative humidity (*RH*) control described in [3]. The *RH* setpoint was first set to 80 or 90%, yielding lamellar phospholipid phases. Then, by lowering *RH*, the samples were dehydrated to induce the stalk phase. The phase behaviour of the lipids was either known from the literature

---

\*Georg-August-Universität Göttingen, Institut für Röntgenphysik, Friedrich-Hund-Platz 1, 37077 Göttingen, Germany

<sup>†</sup>Corresponding Author. E-mail: tsalditt@gwdg.de

[3, 4, 5, 6] or, in case of di-monounsaturated lipids of different chain length structurally similar to DOPC, determined in our laboratory using a setup described in [3] (Fig. S1). The  $RH$  values corresponding to the lamellar/rhombohedral phase boundary of all used lipid compositions are given in Table 1 in the main article. All experiments were performed at room temperature.

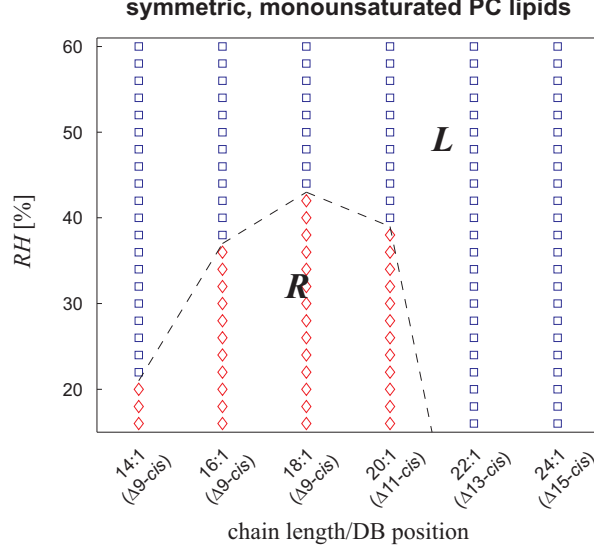


**Figure S1:** Partial phase diagram of symmetric, monounsaturated phosphatidylcholines at room temperature. Several lipids undergo a phase transition from a lamellar phase ( $L$ ) to the stalk phase of rhombohedral symmetry ( $R$ ) upon dehydration. Least osmotic pressure  $\Pi = -(k_B T/v_w) \ln(RH/100\%)$  is required to induce the stalk phase in DOPC (di18:1PC). Absence of the stalk phase in case of very long acyl chains may be related to the fact that these lipids are not in the fluid  $L_\alpha$  phase at room temperature or in dehydrated conditions [7].

### 3 Structure determination of stalks

#### 3.1 X-ray experiments

The goal of the x-ray diffraction experiments is to measure as many Bragg reflections as possible and determine the corresponding form factors  $F_{hkl}$ , which are related to the unit cell electron density  $\rho(\vec{r})$  by the Fourier transform

$$F_{hkl} = \int_V \rho(\vec{r}) \exp(i\vec{q}_{hkl} \cdot \vec{r}) dV. \quad (\text{S1})$$

$V$  denotes the unit cell volume and  $\vec{q}_{hkl}$  the momentum transfer corresponding to a reflection with Miller indices  $h, k, \ell$ . In the following, for the case of oriented samples, the surface normal to the substrate is denoted by  $\vec{e}_z$ . Hence,  $q_{||} = (q_x^2 + q_y^2)^{1/2}$  and  $q_z$  denote the momentum transfer components parallel and perpendicular to the substrate surface, respectively. The experimental method for reconstruction of  $\rho(\vec{r})$  of the stalk phase of phospholipids was pioneered by the group of Huey Huang. An unusual situation arises due to the fact that nonlamellar phases obtained by dehydration of aligned lipid bilayer stacks must be described as two-dimensional powders consisting of crystallites with random in-plane orientation, but aligned with respect to the substrate surface. Measurements in different scattering geometries are therefore required to obtain complete sets of correctly scaled form factors  $\{F_{hkl}\}$  required for electron density reconstruction [4, 5, 8]. In our experiments and subsequent phase retrieval, we adopted this strategy with some modifications. Further details can be found in [9].

*Grazing-incidence x-ray diffraction:* Synchrotron experiments were carried out at the Materials Science beamline (MS-X04SA) at the Swiss Light Source (SLS) at the Paul Scherrer Institute

(PSI, Villigen, Switzerland) using the 2+3-circle surface diffractometer (Micro-Controle Newport) at the surface diffraction endstation (experimental hut 2) with horizontal sample surface orientation. A double-crystal monochromator consisting of two Si(111) crystals was used to select the photon energy of 19.5 keV corresponding to a wavelength of  $\lambda = 0.6358 \text{ \AA}$  from the wiggler beam. The beam was collimated by a set of slits to a size of  $200 \times 50 \mu\text{m}^2$ , yielding a primary intensity of  $2.4 \times 10^{10}$  photons per second. Diffraction patterns were recorded using a Pilatus II pixel detector ( $487 \times 195$  pixels with a size of  $172 \times 172 \mu\text{m}^2$ ) at a distance of  $1140.8 \pm 0.25 \text{ mm}$  from the sample. The path between sample and detector was evacuated by a flight tube. Samples on  $15 \times 10 \text{ mm}^2$  substrates were mounted in a compact home-built chamber with an inner volume of about  $4 \text{ cm}^3$  equipped with polypropylene windows of a thickness below  $1 \mu\text{m}$  to minimize background scattering. After alignment of the substrate surface parallel to the beam and in the beam center, the angle of incidence was set to  $\alpha_i \simeq 0.15^\circ$ . As the Pilatus detector did not subtend the full region where diffraction peaks were visible, a complete diffraction pattern was obtained by combination of four slightly overlapping frames at different detector positions. The exposure for each frame was 30 s. For detector positions recording the diffuse Bragg sheets along the  $q_z$  axis, attenuators were used in order to reduce the signal. This procedure was repeated 3 to 4 times and corresponding frames were added in order to improve the signal-to-noise ratio. After each frame, the sample was translated along the beam to expose a fresh patch and prevent radiation damage. To solve the crystallographic phase problem by the swelling method as described below, data were recorded for several  $RH$  values in the stability range of the rhombohedral phase.

Grazing-incidence data on DOPC/cholesterol samples were recorded in a different experiment at beamline ID01 at the European Synchrotron Radiation Facility (ESRF, Grenoble, France). The photon energy of 17 keV ( $\lambda = 0.7293 \text{ \AA}$ ) was selected from the undulator beam by a double-crystal monochromator composed of two Si(111) crystals. After collimation to a size of  $500 \times 100 \mu\text{m}^2$ , the flux at the sample was about  $1 \times 10^{10}$  photons per second. A Princeton CCD detector ( $1340 \times 1300$  pixels  $48 \times 49 \mu\text{m}^2$  in size) mounted on the detector arm at a distance of  $495.1 \pm 2.4 \text{ mm}$  to the sample was used to record stalk phase diffraction patterns. In the plane of incidence, the specular beam and the first diffuse Bragg sheet were attenuated to avoid detector saturation. Experiments were carried out in the same way as described above, with the exception that the CCD size allowed to record a full diffraction pattern in a single frame. The exposure for each frame was typically limited to 10 s before CCD readout. Several equivalent frames were recorded and added up to improve the signal-to-noise ratio. A typical pattern is shown in Fig. S2.

*X-ray reflectivity:* Additional x-ray reflectivity measurements were used to record the Bragg peaks along the  $q_z$  axis. Experiments were carried out at our institute using a home-built laboratory diffractometer and samples prepared on  $25 \times 15 \text{ mm}^2$  substrates. The x-ray beam was generated by a sealed tube with Cu anode and line focus (Seifert Dx-Cu12 $\times$ 0.4-S long fine focus). A multilayer mirror (Pantak Seifert) was used to parallelize the beam and select the Cu-K $_{\alpha}$  line ( $\lambda = 1.5406 \text{ \AA}$ ). After collimation to a size of  $0.5 \times 6.5 \text{ mm}^2$  by a set of motorized slits, the primary flux was about  $2.3 \times 10^8$  photons per second. Behind the sample, the reflected beam was collimated by two vertical slits of 2 mm and 0.8 mm in width placed directly behind the environmental chamber and in front of the detector (Cyberstar fast scintillation counter, Oxford Danfysik), respectively. For several hydration levels covering the  $RH$  range of the corresponding grazing-incidence data, the specularly reflected intensity was recorded as a function of the incident angle  $\alpha_i$  with a stepsize of  $\Delta\alpha_i = 0.005^\circ$ . Automatic attenuators were used to avoid detector saturation. For all lipids, 7 – 8 Bragg peaks could be recorded. A counting time of 1 s per datapoint was used for the lower orders of diffraction. For higher order Bragg peaks, this was increased to 5 or 10 s to improve the signal-to-noise ratio. The peak width was typically  $0.07^\circ$  (full width at half maximum). In order to speed up the measurements and avoid deterioration of the samples, which was sometimes observed during earlier experiments after longer total exposure to the beam ( $\geq 12 \text{ h}$ ), only the intervals required for integration of the Bragg peaks were recorded in most cases.

*Powder diffraction:* Powder samples were required for relative normalization of the form factor data obtained from grazing-incidence and reflectivity experiments. Powder diffraction patterns were recorded using a home-built small-angle x-ray scattering instrument described in [3]. Cu-K $_{\alpha}$  radiation was generated by a sealed tube with point focus (Seifert FK61-04 $\times$ 12Cu) and monochro-

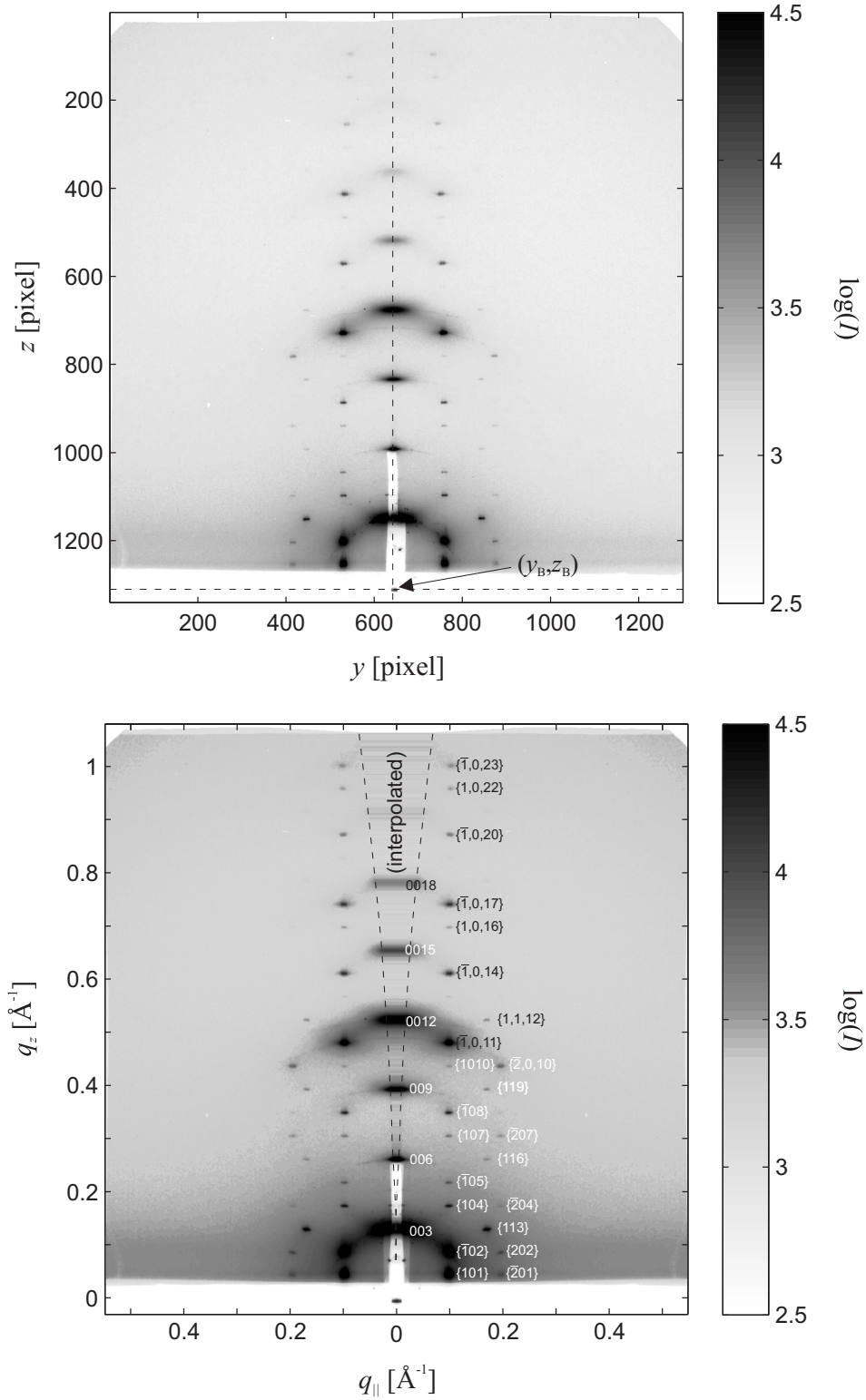


**Figure S2:** GIXD diffraction pattern recorded at ID01 (DOPC/cholesterol 70:30, RH = 60%, sum of 50 frames of 10 s exposure) (top) and corresponding intensity distribution obtained after polarization correction, left/right averaging, smoothing by a  $3 \times 3$  box filter and transformation to the  $(q_{||}, q_z)$  plane (bottom). For the Miller indices  $\{hkl\}$ , see also Tab. S1.

matized by a multilayer mirror (Xenocs Fox 2D Cu 12Inf). After collimation by two pinholes (diameter 1 mm), a primary intensity of about  $1.8 \times 10^8$  photons per second was measured at the sample position by a Forvis PIN diode. For data collection, a Bruker HiStar area detector (multiwire proportional counter) located  $867.9 \pm 1.8$  mm behind the sample (determined by the calibration standard silver behenate) was used. A beamstop placed directly behind the sample removed the primary beam and thus reduced background scattering by air. Powder diffraction patterns as shown in Fig. S3b were recorded for several  $RH$  values covering the  $RH$  range of the corresponding grazing-incidence data. For each frame, the exposure was typically 4 hours. The phase boundaries between the lamellar and rhombohedral phases for powder samples were in agreement with those found for the oriented samples.

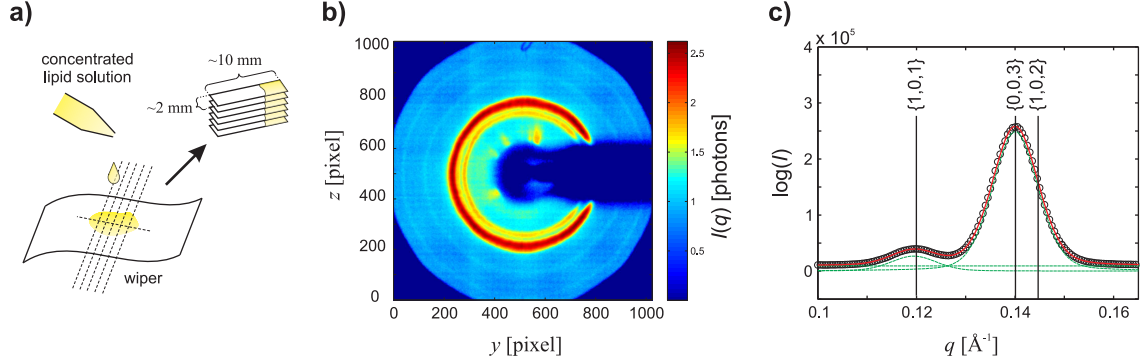


**Figure S3:** (a) Preparation of powder samples, (b) powder diffraction pattern of the rhombohedral phase of DPhPC ( $RH = 76\%$ ) and (c) radially integrated intensity and peak fitting of the  $\{1,0,1\}$  and the overlapping  $\{0,0,3\}$  and  $\{1,0,2\}$  reflections.

### 3.2 Data reduction

The reflections were indexed as shown in Fig. S2 (*bottom*) using a nonprimitive hexagonal unit cell spanned by vectors  $(a, 0, 0)^T$ ,  $(-\frac{a}{2}, \frac{\sqrt{3}a}{2}, 0)^T$  and  $(0, 0, 3d)^T$ . Each reflection then corresponds to the momentum transfer

$$\vec{q}_{hkl} = 2\pi \left( \frac{h}{a}, \frac{2k+h}{\sqrt{3}a}, \frac{\ell}{3d} \right)^T. \quad (\text{S2})$$

Bragg peaks are only observed if they fulfill the reflection condition  $-h + k + \ell = 3n$ ,  $n \in \mathbb{Z}$  indicating rhombohedral symmetry [13]. Raw data files recorded in grazing-incidence geometry were corrected for detector sensitivity and dead pixels and subsequently composed to full diffraction patterns (in case of SLS data), corrected for polarization and transformed to the  $q_{||}$ ,  $q_z$  plane. Bragg peaks are located in several series parallel to the  $q_z$  axis with ratios of  $1:\sqrt{3}:2:\sqrt{7}:3$  in  $q_{||}$ . Peaks of the two outer series were not observed for all lipids and were sufficiently strong for further analysis only in case of DPhPC at  $RH \leq 70\%$ . The lattice parameter  $d$  was determined from the maxima of the first five diffuse Bragg sheets along the  $q_z$  axis, the lattice parameter  $a$  from the positions of Bragg peaks where  $q_{||} \neq 0$ . For each peak series with  $q_{||} = \text{const.}$ , the intensity was integrated in  $q_{||}$  direction. The integrated intensities were then determined as the corresponding peak areas in the obtained one-dimensional intensity profiles. Coinciding reflections are assumed to be symmetry-equivalent and possess same form factor [5]. The corresponding integrated intensities were divided by the peak multiplicity and corrected for the Lorentz factor, finally yielding  $K_{\text{OPR}} \cdot |F_{hkl}|$  for all out-of-plane reflections where  $q_{||} \neq 0$ , *i.e.* not in the plane of incidence.  $K_{\text{OPR}}$  denotes an unknown scaling factor which incorporates *e.g.* primary beam intensity, duration of the exposure, size and number of the diffracting crystalline domains, and detector sensitivity.

Reflectivity curves were corrected for polarization, absorption and illumination effects and plotted as a function of momentum transfer  $q_z = \frac{4\pi}{\lambda} \sin \alpha_i$  perpendicular to the substrate plane. Lattice constants  $d$  were determined from the Bragg peak positions  $q_{00\ell} = 2\pi\ell/3d$ . Using the small-angle

approximation of the Lorentz correction factor for oriented samples, the integrated peak intensities yield the form factor amplitudes  $K_{\text{IPR}} \cdot |F_{00\ell}| = \sqrt{\ell \cdot I_{00\ell}}$  up to another unknown scaling factor  $K_{\text{IPR}}$  (in-plane reflections). To obtain matching  $d$  values for the corresponding grazing-incidence data, we performed a linear interpolation of each form factor amplitude as a function of the lattice parameter  $d$ .

Due to the two unknown scaling factors  $K_{\text{IPR}}$  and  $K_{\text{OPR}}$ , it is not straightforward to put the form factors of in-plane and out-of-plane reflections onto a common scale. Notably, this step is of great importance, since an incorrect relative normalization of both groups of form factors would distort the final structures and corrupt the results of a further quantitative analysis. We solved this issue by additional powder diffraction patterns, a different procedure is discussed in [5, 8].

Raw images were radially integrated to obtain the one-dimensional intensity profile  $I(q)$  (Fig. S3c). The double peak at approx.  $q = 0.12 \text{ \AA}^{-1}$  was fitted with a pair of pseudo-Voigt peaks of the same width and mixing parameter. The fit parameters, combined with the ratio of the form factor amplitudes  $|F_{101}|/|F_{102}|$  known from the grazing-incidence data, yield the integrated intensities corresponding to the  $\{101\}$  and  $\{003\}$  reflections. These were subsequently corrected for peak multiplicity and by Lorentz and polarization correction factors for the powder case [10], and finally provide the ratio  $|F_{101}|/|F_{003}|$ . The used equations can be found in [9]. In addition, the form factor corresponding to the  $\{110\}$  reflection, which is absorbed by the substrate in grazing-incidence geometry, was obtained from the powder patterns. Using powder data for different  $RH$  levels, the ratios  $|F_{101}|/|F_{003}|$  and  $|F_{110}|/|F_{003}|$  were obtained for the stalk phase as a function of  $d$  by linear interpolation. Finally, these were used for relative normalization of grazing-incidence and reflectivity data and completion of the datasets by the form factor amplitude  $|F_{110}|$ .

### 3.3 Solving the phase problem

Having obtained all measureable form factor amplitudes  $\{|F_{hkl}|\}$  on a common scale, the next step is to solve the crystallographic phase problem. In general, the form factors are complex numbers  $|F_{hkl}|\exp(i\phi_{hkl})$ . The phase angles  $\phi_{hkl} \in [0, 2\pi]$  are not directly accessible from the measured intensities. Lipid mesophases are treated as centrosymmetric (*e.g.* [11, 12]), which reduces the phase problem with infinitely many solutions to the sign problem  $F_{hkl} = \nu_{hkl}|F_{hkl}|$  with phase factors  $\nu_{hkl} = \pm 1$  and a finite number of  $2^N$  possible phase combinations.  $N$  denotes the number of independent reflections.

For each lipid, the phase factors  $\{\nu_{hkl}\}$  were determined by the swelling method using the datasets of different hydration levels or  $d$  values, respectively. In case of lamellar phases, the swelling method is based on the idea that small changes in hydration mainly affect the thickness of water layers between adjacent bilayers, while the bilayer structure itself remains approximately constant. For rhombohedral phases, this assumption must be relaxed to some extent, since there is no obvious way to shrink a three-dimensional unit cell without changes in the contained lipid structure. Nevertheless, using the swelling method for the rhombohedral phase [4, 5], sign combinations  $\{\nu_{hkl}\}$  leading to very reasonable lipid distributions in the unit cell could be found.

To this end, each peak series parallel to the  $q_z$  axis was treated separately. The corresponding form factors were normalized so that  $(2\pi/d) \cdot \sum_{\ell} |F_{hkl}|^2 = \text{const.}$  for the different levels of hydration. For the series with  $q_{\parallel} = 0$  obtained from reflectivity data, the form factor amplitudes are less subject to experimental errors than the ones obtained from grazing-incidence data. This is due to the  $2d$  powder character of the samples: In the reflectivity scans where  $\vec{q} \parallel \vec{e}_z$ , all domains contribute to the Bragg peak intensity, while in grazing-incidence only a small fraction with suitable in-plane orientation does. To suppress possible outliers, each group of amplitudes  $F_{hkl}$  was fitted by a straight line and subsequently replaced by the linearized values. Then, for all possible sign combinations, the continuous transforms

$$F(\vec{q}_{hk}, q_z) = \sum_{\ell} \nu_{hkl} |F_{hkl}| \frac{\sin\left(\frac{d}{2}q_z - \frac{\pi}{3}\ell\right)}{\frac{d}{2}q_z - \frac{\pi}{3}\ell}, \quad h, k = \text{const.} \quad (\text{S3})$$

were calculated using the average values of  $d$  and each amplitude  $|F_{hkl}|$ . The phase combination leading to the best agreement of the discrete datapoints and the continuous transform, indicated

by the minimum residual sum of squares, was then considered the most reasonable choice. All swelling diagrams are provided below.

Considering the obtained phase combinations, we note the following: In each series, the signs  $\{\nu_{hk\ell}\}$  are typically alternating, *i.e.* signs of two adjacent reflections with  $h, k$  fixed and  $\Delta\ell = 3$  are different in most cases. This is related to the triplet relationship for centrosymmetric structures used in direct methods for crystallography: It can be shown that the signs corresponding to three reflections with

$$\sum_{i=1}^3 \vec{q}_{h_i k_i \ell_i} = 0 \quad (\text{S4})$$

are likely to fulfill the condition

$$\prod_{i=1}^3 \nu_{h_i k_i \ell_i} = +1 \quad (\text{S5})$$

if the corresponding  $|F_{h_i k_i \ell_i}|$  are all relatively strong [13]. In all of our datasets, the form factor amplitude  $|F_{003}|$  corresponding to the first Bragg peak in the reflectivity scans is by far the strongest one. Electron density maps with one continuous region of elevated electron density indicative of lipid headgroups separating two continuous regions of lower electron density such as the water and hydrocarbon regions are only obtained if  $\nu_{003} = -1$ . For a triplet containing  $\{003\}$ , the remaining two reflections are adjacent ones within one peak series, *i.e.*  $h, k = \text{const.}$  and  $\Delta\ell = 3$ . Hence, these are likely to have opposite signs, especially if they are both relatively strong as well. Therefore, only phase combinations with  $\nu_{003} = -1$  and  $\nu_{101} = -\nu_{102}$  were used for the swelling method.

Subsequent to determination of the  $\{\nu_{hk\ell}\}$  within each series  $h, k = \text{const.}$  by the swelling method, the relative phases between the four series were determined by considering all 8 possible electron density maps  $\Delta\rho(0, y, z)$  and choosing the only one which leads to physically reasonable electron density distributions compatible with continuous lipid headgroup and hydrocarbon regions. For all lipids under investigation, the obtained phase combinations are very similar. The phase factors  $\{\nu_{11\ell}\}$  where  $\ell = 3, 6, 9, 12$  were unambiguously obtained as  $+-++$  for all lipids. For the  $\{110\}$  reflection determined from the powder measurements, we then used  $\nu_{110} = -\nu_{113}$ , in agreement with Eq. S5. A slight ambiguity arose for the phase factors  $\{\nu_{20\ell}\}$  where  $\ell = -2, 1, 4, 7, 10$ . For different datasets, both  $+-+-+$  and  $---+-$  were obtained as the best combinations according to the swelling method. Based on the corresponding electron density maps in the  $xy$  plane, we used the former choice because it leads to a more homogeneous and radially symmetric electron density in the lipid headgroup region. All form factors and corresponding lattice parameters at different hydration levels are provided below. The phase factors  $\nu_{hk\ell}$  are very similar for all datasets. The electron density contrast  $\Delta\rho(\vec{r})$  was then reconstructed by the Fourier cosine series

$$\Delta\rho(\vec{r}) = \sum_{h,k,\ell} \nu_{hk\ell} |F_{hk\ell}| \cos(\vec{q}_{hk\ell} \cdot \vec{r}). \quad (\text{S6})$$

In all cases, we obtain density maps which are compatible with two regions of lower electron density contrast (hydrocarbon/water) separated by a continuous region of increased electron density contrast (lipid headgroups) as required due to the hydrophobic effect, and clearly display the characteristic shape of a stalk.

## 4 Bilayer electron density profiles

Oriented lamellar phases are characterized by a single series of equidistant Bragg peaks indexed by  $n = 1, 2, \dots$  along the  $q_z$  axis. Reflectivity scans are therefore sufficient to record all crystallographic data required for determination of bilayer structure and interactions. Experiments and extraction of lattice parameters  $d$  and form factor amplitudes  $|F_n|$  (up to an unknown constant factor) were carried out as described above. We then used the well-established swelling method for lamellar phases (*e.g.* [14] and references therein) to determine the phase factors  $\nu_n = \pm 1$ . The continuous form factor (Eq. S3) simplifies to

$$F(q_z) = \sum_n \nu_n |F_n| \frac{\sin\left(\frac{d}{2}q_z - n\pi\right)}{\frac{d}{2}q_z - n\pi}. \quad (\text{S7})$$

Finally, electron density profiles were reconstructed on arbitrary scale by

$$\Delta\rho(z) = \sum_{n=1}^N \nu_n |F_n| \cos\left(n\frac{2\pi}{d}\right). \quad (\text{S8})$$

Based on this structural information, the hydration forces per unit area were determined as described in the main article. Here, we describe some additional observations at small bilayer separation, *i.e.* close to the  $L/R$  phase boundary, and explain the choice of the  $RH$  interval used for hydration force determination:

For most lipids, data were recorded over a  $RH$  interval covering both  $L$  and  $R$  phases. Upon dehydration, the lattice constant  $d$  decreases monotonously. Only in case of DPhPC (Fig. S4a, compare also [15]), two series of Bragg peaks indicating phase coexistence could be clearly resolved at  $RH$  close to the  $L/R$  phase boundary. For all other lipids, the phase transition was rather indicated by shoulders of the Bragg peaks similar to the example shown in Fig. S4b. The corresponding  $RH$  values are in agreement with phase diagram data [3, 6].

Distinct regimes can be recognized in the curves  $d(RH)$  (Fig. S4c): The rate  $\left|\frac{\partial d}{\partial RH}\right|$  changes in a non-monotonous fashion, and  $d(RH)$  is characterized by two inflection points. The one at lower  $RH$  is in very good agreement with the  $L/R$  phase boundary of the respective sample. In the  $RH$  interval between these two points, termed “transition region” in Fig. S4c, the following observations indicate changes in the bilayer stack:

As shown in Fig. S4d for pure DOPC, a drop of the form factor amplitudes of the higher-order reflections is visible at  $RH \leq 60\%$ . Agreement of the sampled form factor amplitudes  $|F_n|$  and the continuous form factor reconstructed by Eq. S7 becomes significantly worse in the transition region. Except for DPhPC, a similar effect could be observed for all samples. Fig. S4e shows GIXD data on DOPC in the corresponding hydration interval. Upon lowering  $RH$  and prior to appearance of out-of-plane reflections indicating the  $R$  phase, the shape of the diffuse Bragg sheets begins to change and considerable diffuse precursors appear around the position of future out-of-plane reflections. This effect was observed in DOPC during both synchrotron beamtimes. As a working hypothesis, we propose that it could result from the formation of transient stalks which do not yet possess long-range positional correlations such as in the stalk phase.



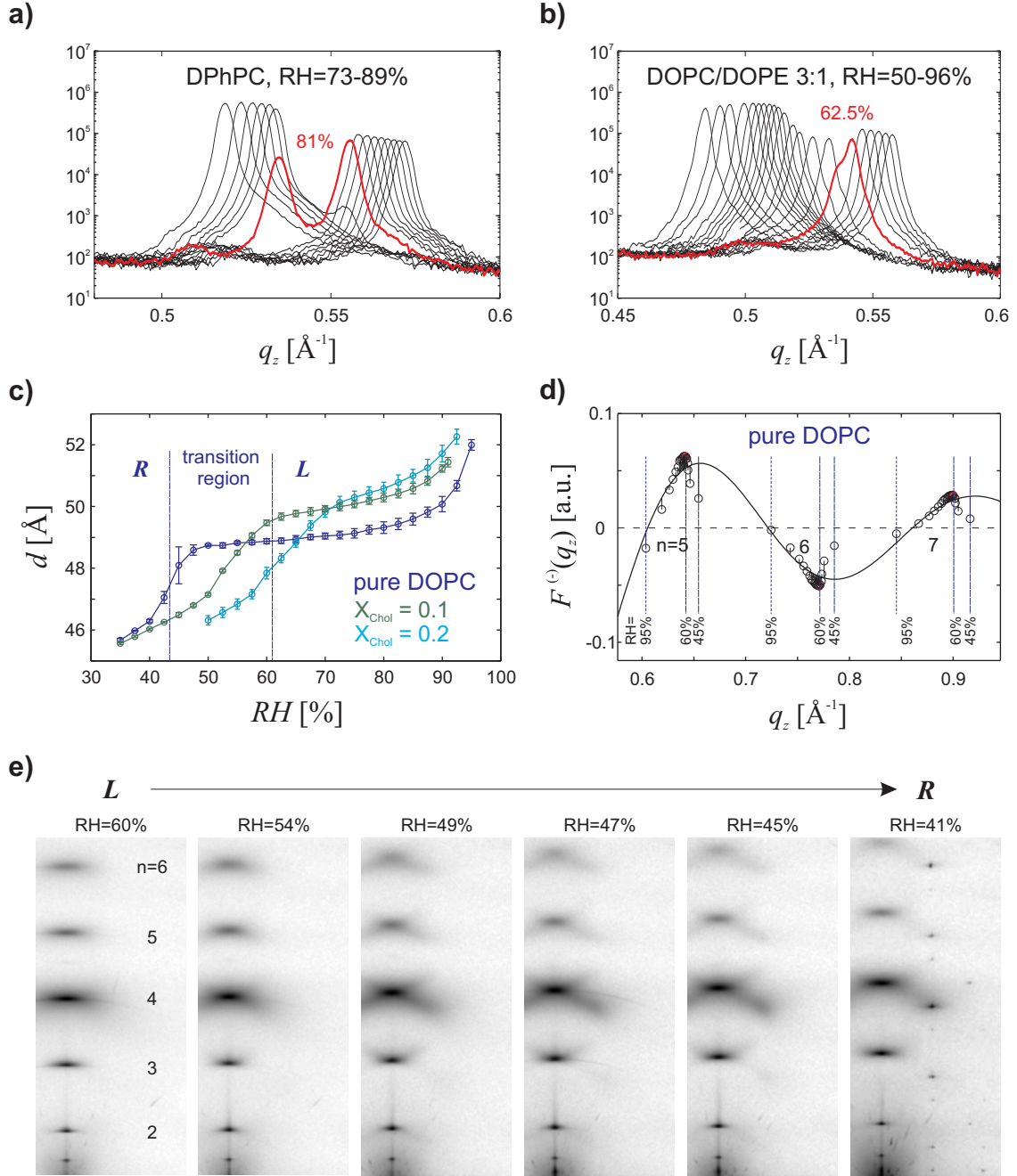


**Figure S4:** (a) 4th Bragg peaks of DPhPC and (b) DOPC/DOPE 3:1 in RH intervals covering the L and R phases. Curves indicating the L/R phase transition are shown in red. (c) Lattice constant  $d$  in DOPC/Chol mixtures. Dashed vertical lines indicate the approximate inflection points of the curve  $d(\text{RH})$  of DOPC. (d) In this transition region, agreement of the discrete samples  $|F_{n,\text{RH}}|$  and the continuous form factor reconstructed from all datapoints in the L phase becomes worse. (e) Also GIXD patterns (SLS beamtime) in this interval indicate structural changes. The shape of the Bragg sheets changes and considerable diffuse scattering becomes visible at RH levels slightly above the appearance of sharp out-of-plane reflections.

## 5 Electron density isosurface analysis

Here we describe the algorithm used for extraction of the curvature properties of electron density isosurfaces defined by the implicit function

$$f(\vec{r}) = \Delta\rho(\vec{r}) - \rho_{\text{iso}} = 0. \quad (\text{S9})$$

The coordinates  $(x, y)$  within the hexagonal base corresponding to one stalk were discretized on a grid with  $\Delta x = \Delta y = 0.25 \text{ \AA}$ .  $\Delta\rho(\vec{r})$  was reconstructed using the typically 25 reflections whose phases  $\nu_{hkl} = \pm 1$  could be unambiguously determined. These are provided in the form factor tables below. For each point  $(x, y)$ , the  $z$  value such that  $f(\vec{r}) = 0$  was computed numerically (Fig. S5). The area of the corresponding surface patch is

$$\Delta A = \frac{|\nabla f|}{|\partial_z f|} \Delta x \Delta y. \quad (\text{S10})$$

The gradient

$$\nabla f = - \sum_{h,k,\ell} \nu_{hkl} |F_{hkl}| \sin(\vec{q}_{hkl} \cdot \vec{r}) \cdot \vec{q}_{hkl}, \quad (\text{S11})$$

the Hessian

$$\text{Hess}(f) = -4\pi^2 \sum_{h,k,\ell} \nu_{hkl} |F_{hkl}| \cos(\vec{q}_{hkl} \cdot \vec{r}) \cdot \begin{pmatrix} \frac{h^2}{a^2} & \frac{h(2k+h)}{\sqrt{3}a^2} & \frac{h\ell}{3ad} \\ \frac{h(2k+h)}{\sqrt{3}a^2} & \frac{(2k+h)^2}{3a^2} & \frac{(2k+h)\ell}{3\sqrt{3}ad} \\ \frac{h\ell}{3ad} & \frac{(2k+h)\ell}{3\sqrt{3}ad} & \frac{\ell^2}{9d^2} \end{pmatrix} \quad (\text{S12})$$

and the area element

$$\Delta A = \frac{\left| \sum_{h,k,\ell} \nu_{hkl} |F_{hkl}| \cdot \sin(\vec{q}_{hkl} \cdot \vec{r}) \cdot \vec{q}_{hkl} \right|}{\left| \sum_{h,k,\ell} \nu_{hkl} |F_{hkl}| \cdot \sin(\vec{q}_{hkl} \cdot \vec{r}) \cdot \frac{2\pi}{3d} \ell \right|} \Delta x \Delta y \quad (\text{S13})$$

obtained from Eq. S6 can be written as linear combinations of sines or cosines using the experimentally determined form factor amplitudes  $|F_{hkl}|$  and corresponding phases  $\nu_{hkl} = \pm 1$ . The adjugate of the Hessian is determined by the cofactor relation  $(\text{Hess}^*(f))_{ij} = (-1)^{i+j} M_{ij}$ , where the minor  $M_{ij}$  denotes the determinant of the  $2 \times 2$  matrix obtained by cancelling row  $i$  and column  $j$  of  $\text{Hess}(f)$ . With these relations, the mean and Gaussian curvature  $H$  and  $K$  of each surface patch were determined using Eq. 6 and 7 in the main article. To improve the accuracy of the final results, the stalk neck region around  $x^2 + y^2 = (d_s/2)^2$  where the strongest bending occurs was resampled using a finer grid of  $0.05 \text{ \AA}$  in  $(x, y)$ . Integrations yielding  $\Sigma_1$ ,  $\Sigma_2$  the monolayer area  $A$  and  $\int_A K dA$  were performed by summation over all area elements. Finally, using centrosymmetry, the results were multiplied by a factor of 2 to take into account the full *cis* monolayer corresponding to one stalk. All computations were carried out in MATLAB [16].

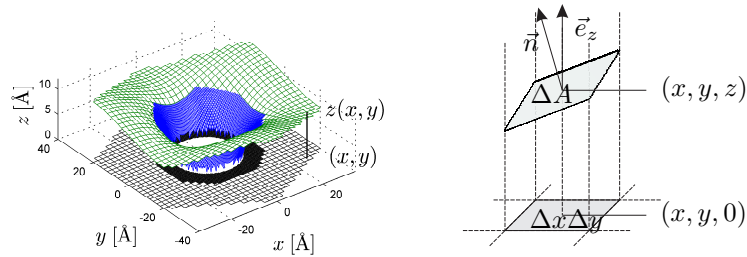


**Figure S5:** (left) Isosurface determination: The hexagonal base corresponding to one stalk is discretized. For each point  $(x, y)$  of the grid, the height  $z(x, y)$  such that  $f(x, y, z(x, y), \rho_{\text{iso}}) = 0$  is determined numerically (green). For higher accuracy, the strongly curved region was subsequently resampled using a finer grid (blue). For the presented results, the sampling was considerably finer than shown here. (right) Sketch of an area element in the  $xy$  plane and corresponding isosurface patch  $\Delta A$ .

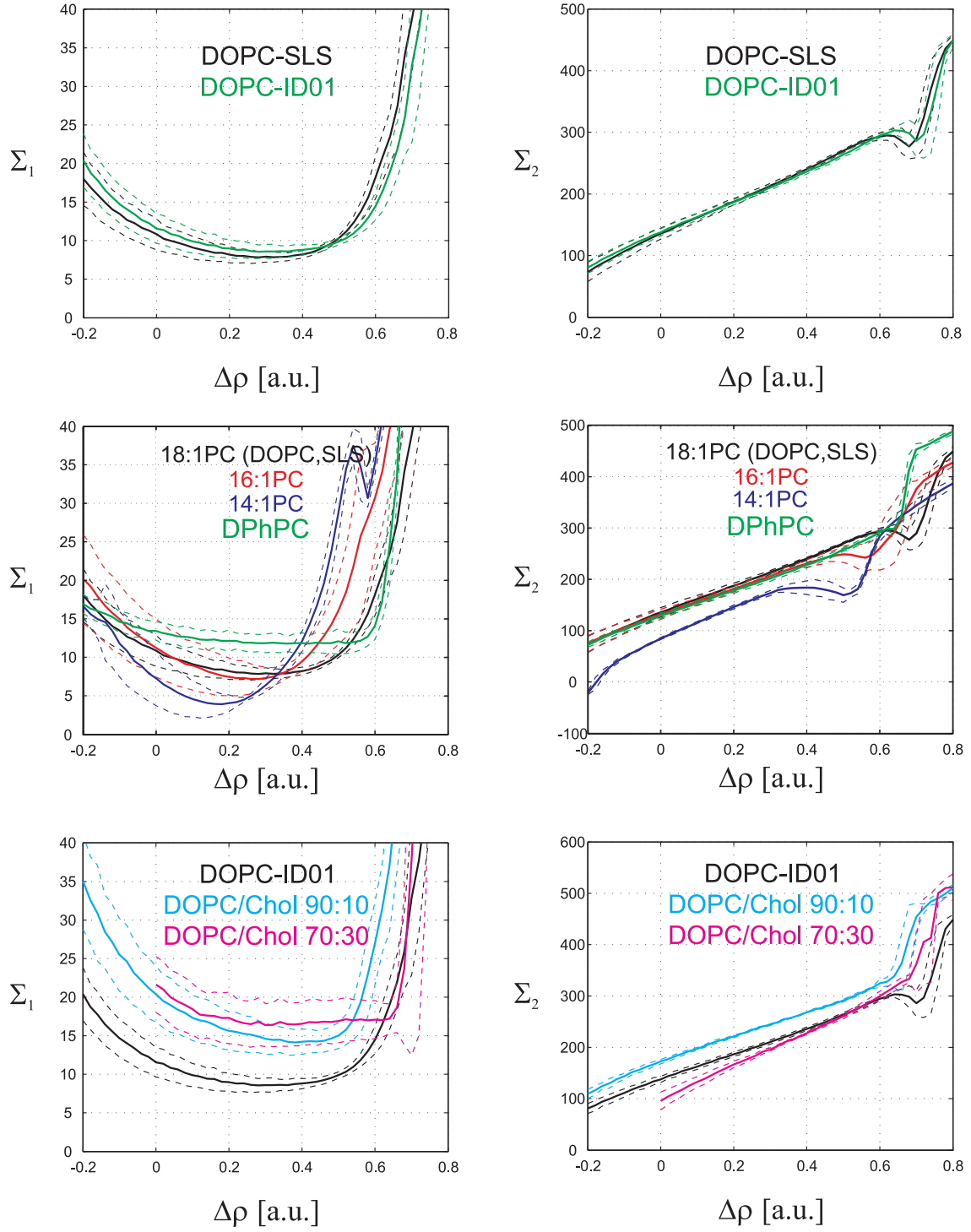


**Figure S6:** Results for  $\Sigma_{1,2}$  obtained by electron density isosurface analysis. The results for DOPC including grazing-incidence data from two different synchrotron measurements agree within error bars. An increase in chain length or addition of cholesterol successively shift the minimum of  $\Sigma_1$  to higher  $\Delta\rho$ . In case of DOPC and 30 mol% cholesterol (bottom row), isosurfaces exhibit stalk-like topology only for  $\Delta\rho > 0$ .

## 6 Form factor and swelling data

Below, all swelling diagrams and corresponding form factor data are provided. The following points should be noted:

- As summarized in Tab. S1, a family of equivalent reflections is denoted by a single index triplet  $\{hkl\}$ .
- The form factors for each  $RH$  level are normalized such that  $\max \Delta\rho = 1$  in the resulting electron density distributions.
- Reflections which were not used in electron density isosurface analysis are indicated by an asterisk \*.
- As explained above, deviations between swelling plots and form factor tables occur for some lipids in case of the  $\{02\ell\}$  reflections, since the best combination according to the swelling method did not always yield the most reasonable  $\Delta\rho(\vec{r})$ .
- Datapoints corresponding to the strong  $|F_{003}|$  reflection with  $\nu_{hkl} = -1$  are not shown in order to increase the visibility of the substantially weaker higher orders of the  $\{00\ell\}$  series.
- The number of hydration levels used in reflectivity and GIXD data was different in most cases. Therefore, the number of datapoints in the swelling diagrams of in-plane and out-of-plane reflections may be different.
- Datasets for DOPC, DPhPC and DOPC/DOPE 1:1 recorded during the SLS beamtime are each composed of data from two samples. Therefore, some  $RH$  values may occur twice and, in case of DOPC, even in non-monotonous order. We attribute this to the limited precision of the used  $RH$  sensor and to sample history.
- For the two DOPC datasets (SLS/ESRF) from two synchrotron beamlines, the same reflectivity (and powder) data were used. Therefore, the swelling plots for the  $\{00\ell\}$  series are the same in both figures.

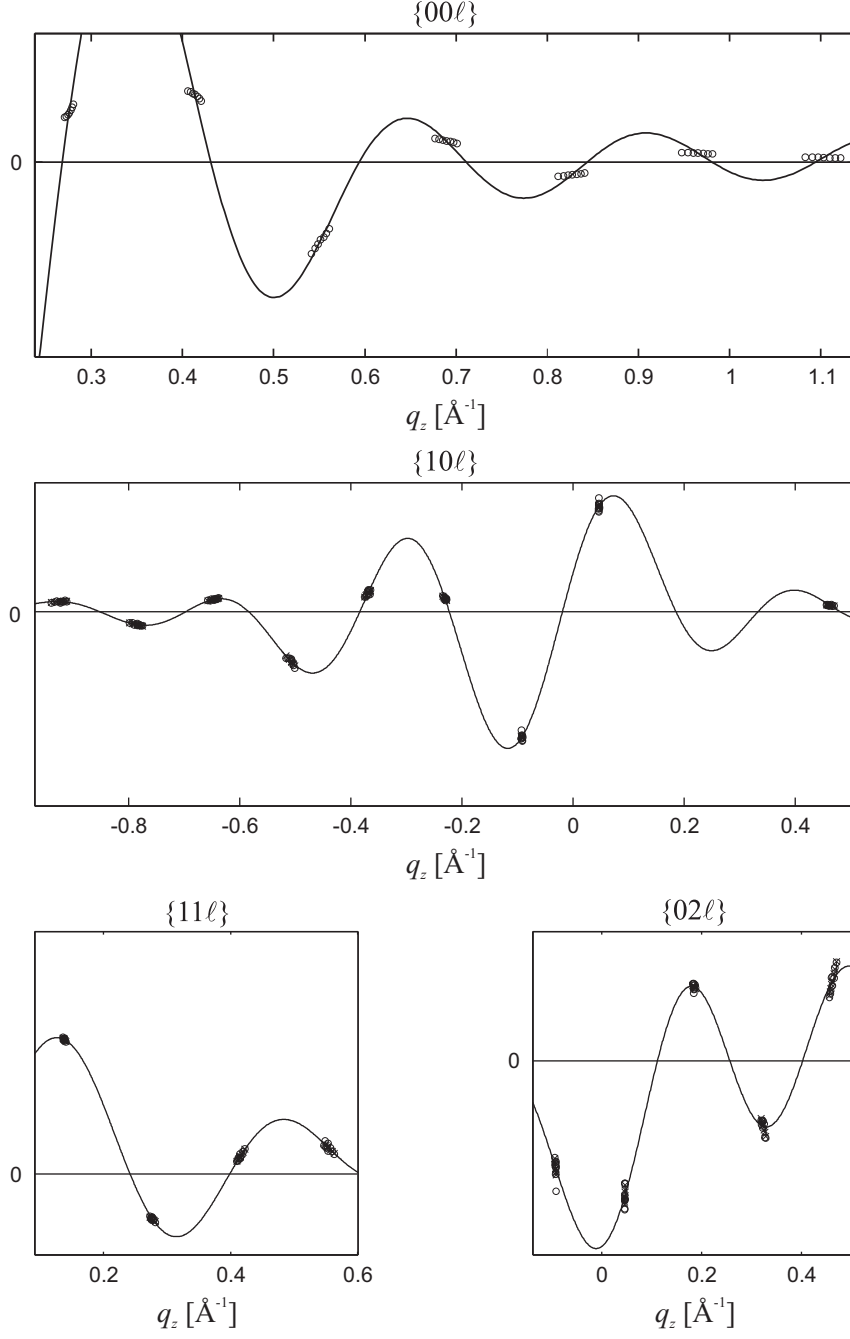
family	reflections	$q_{  }/\frac{4\pi}{\sqrt{3}a}$
$\{00\ell\}$	$(00\ell)$	0
$\{10\ell\}$	$(10\ell), (0\bar{1}\ell), (\bar{1}1\ell)$	1
$\{11\ell\}$	$(11\ell), (\bar{1}\bar{1}\ell), (2\bar{1}\ell), (\bar{2}1\ell), (1\bar{2}\ell), (\bar{1}2\ell)$	$\sqrt{3}$
$\{02\ell\}$	$(02\ell), (\bar{2}0\ell), (2\bar{2}\ell)$	2
$\{21\ell\}$	$(21\ell), (3\bar{1}\ell), (1\bar{3}\ell), (\bar{1}\bar{2}\ell), (\bar{2}3\ell), (\bar{3}2\ell)$	$\sqrt{7}$
$\{30\ell\}$	$(30\ell), (\bar{3}0\ell), (03\ell), (0\bar{3}\ell), (3\bar{3}\ell), (\bar{3}3\ell)$	3

**Table S1:** Families of symmetry-equivalent reflections  $\{hkl\}$  and their members  $(hkl)$  of the rhombohedral phase (non-primitive hexagonal unit cell) as well as the corresponding lateral momentum transfer component  $q_{||}$ .

## References

- [1] Seul, M., Sammon, M.J.: Preparation of Surfactant Multilayer Films on Solid Substrates by Deposition from Organic Solution. *Thin Solid Films* 1990 **185** 287-305.
- [2] Pan, J.J., Tristram-Nagle, S., Kucerka, N., Nagle, J.F.: Temperature Dependence of Structure, Bending Rigidity, and Bilayer Interactions of Dioleoylphosphatidylcholine Bilayers. *Biophys. J.* 2008 **94** 117-124.
- [3] Aeffer, S., Reusch, T., Weinhausen, B., Salditt, T.: Membrane fusion intermediates and the effect of cholesterol: An in-house X-ray scattering study. *Eur. Phys. J. E* 2009 **30** 205-214.
- [4] Yang, L., Huang, H.W.: Observation of a Membrane Fusion Intermediate Structure. *Science* 2002 **297** 1877-1879.
- [5] Yang, L., Huang, H.W.: A Rhombohedral Phase of Lipid Containing a Membrane Fusion Intermediate Structure. *Biophys. J.* 2003 **84** 1808-1817.
- [6] Yang, L., Ding, L., Huang, H.W.: New Phases of Phospholipids and Implications to the Membrane Fusion Problem. *Biochemistry* 2003 **42** 6631-6635.
- [7] Koynova, R., Caffrey, M.: Phases and phase transitions of the phosphatidylcholines. *Biochim. Biophys. Acta* 1998 **1376** 91-145.
- [8] Ding, L., *et al.*: Diffraction Techniques for Nonlamellar Phases of Phospholipids. *Langmuir* 2004 **20** 9262-9269.
- [9] Aeffer, S.: *Stalk Structures in Lipid Bilayer Fusion Studied by X-ray Diffraction*. PhD thesis, Georg-August-Universität Göttingen 2011.
- [10] Als-Nielsen, J., McMorrow, D.: *Elements of Modern X-ray Physics*. Wiley 2001.
- [11] Harper, P.E., Mannock, D.A., Lewis, R.N.A.H., McElhaney, R.N., Gruner, S.M.: X-Ray Diffraction Structures of Some Phosphatidylethanolamine Lamellar and Inverted Phases. *Biophys. J.* 2001 **81** 2693-2706.
- [12] Qian, S., Wang, W., Yang, L., Huang, H.W.: Structure of transmembrane pore induced by Bax-derived peptide: Evidence for lipidic pores. *Proc. Nat. Acad. Sci. USA* **105** 17379-17383.
- [13] Massa, W.: *Crystal Structure Determination*. Springer 2001.
- [14] Ghosh, S.K., Aeffer, S., Salditt, T.: Effect of PIP<sub>2</sub> on Bilayer Structure and Phase Behavior of DOPC: An X-ray Scattering Study. *Chem. Phys. Chem.* 2011 **12** 2633-2640.
- [15] Hung, W.C., Chen, F.Y., Huang, H.W.: Order-disorder transition in bilayers of diphytanoyl phosphatidylcholine. *Biochim. Biophys. Acta* 2000 **1467** 198-206.
- [16] Matlab R2008b, The MathWorks.

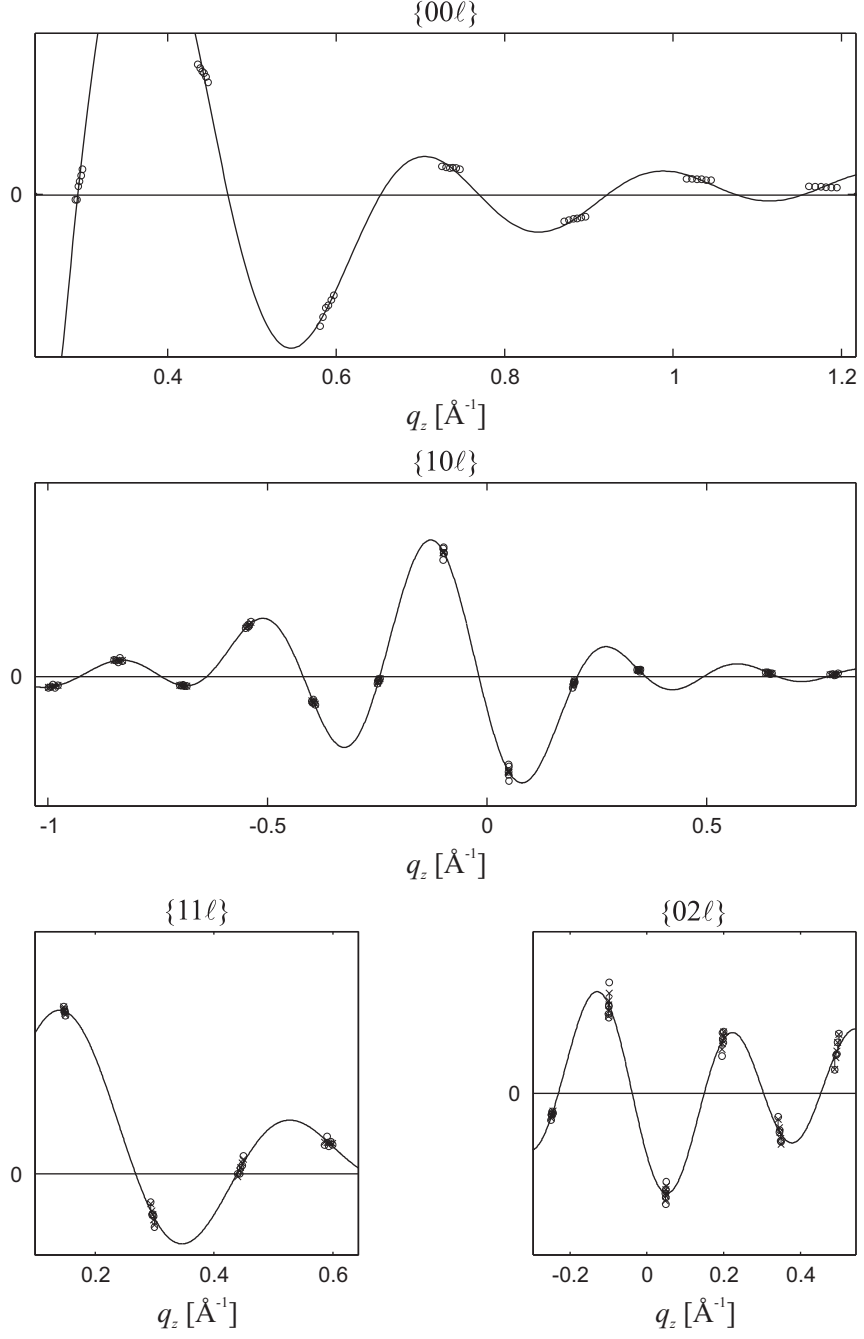
di18:1PC/DOPC (SLS),  $RH = 18 - 34\%$



di18:1PC/DOPC (SLS),  $RH = 18 - 34\%$

$RH$	18	21	24	28	27	30	32	30	34
$d$	44.59	44.89	45.07	45.40	45.41	45.49	45.66	45.79	45.95
$\sigma(d)$	0.07	0.22	0.07	0.15	0.20	0.16	0.16	0.30	0.13
$a$	63.47	64.53	65.49	66.49	66.66	66.90	67.74	68.21	68.89
$\sigma(a)$	0.19	0.14	0.01	0.01	0.14	0.08	0.22	0.08	0.08
<hr/>									
{0, 0, 3}	-0.6295	-0.6468	-0.6717	-0.6790	-0.6759	-0.6803	-0.6760	-0.6785	-0.6930
{0, 0, 6}	0.0431	0.0423	0.0428	0.0410	0.0408	0.0405	0.0391	0.0383	0.0381
{0, 0, 9}	0.0451	0.0476	0.0502	0.0522	0.0520	0.0527	0.0531	0.0539	0.0557
{0, 0, 12}	-0.0474	-0.0520	-0.0560	-0.0603	-0.0601	-0.0615	-0.0630	-0.0647	-0.0679
{0, 0, 15}	0.0136	0.0146	0.0156	0.0164	0.0164	0.0167	0.0169	0.0173	0.0180
{0, 0, 18}	-0.0080	-0.0086	-0.0092	-0.0098	-0.0098	-0.0099	-0.0101	-0.0103	-0.0108
{0, 0, 21}	0.0060	0.0063	0.0067	0.0070	0.0070	0.0071	0.0071	0.0072	0.0075
{0, 0, 24}* {1, 0, 20}* {1, 0, 17}	0.0029 0.0114 -0.0141	0.0031 0.0121 -0.0137	0.0033 0.0119 -0.0146	0.0035 0.0100 -0.0132	0.0035 0.0115 -0.0152	0.0035 0.0111 -0.0144	0.0036 0.0113 -0.0151	0.0037 0.0125 -0.0153	0.0038 0.0106 -0.0145
{1, 0, 14}	0.0144	0.0131	0.0142	0.0132	0.0134	0.0137	0.0139	0.0141	0.0145
{1, 0, 11}	-0.0593	-0.0567	-0.0523	-0.0522	-0.0543	-0.0541	-0.0578	-0.0577	-0.0588
{1, 0, 8}	0.0189	0.0183	0.0188	0.0231	0.0189	0.0237	0.0235	0.0186	0.0225
{1, 0, 5}	0.0204	0.0174	0.0165	0.0139	0.0134	0.0139	0.0128	0.0135	0.0126
{1, 0, 2}	-0.1619	-0.1549	-0.1331	-0.1366	-0.1393	-0.1347	-0.1445	-0.1386	-0.1301
{1, 0, 1}	0.1319	0.1275	0.1275	0.1197	0.1190	0.1174	0.1120	0.1088	0.1067
{1, 0, 7}	-0.0042	-0.0040	-0.0051	-0.0071	-0.0047	-0.0078	-0.0077	-0.0068	-0.0086
{1, 0, 10}* {1, 1, 0}	0.0075 -0.0300	0.0069 -0.0296	0.0079 -0.0300	0.0070 -0.0289	0.0066 -0.0288	0.0070 -0.0286	0.0069 -0.0277	0.0076 -0.0273	0.0072 -0.0272
{1, 1, 3}	0.0269	0.0260	0.0240	0.0239	0.0240	0.0234	0.0242	0.0232	0.0227
{1, 1, 6}	-0.0099	-0.0089	-0.0083	-0.0079	-0.0077	-0.0080	-0.0079	-0.0077	-0.0071
{1, 1, 9}	0.0051	0.0043	0.0034	0.0029	0.0028	0.0034	0.0028	0.0023	0.0021
{1, 1, 12}	0.0040	0.0044	0.0046	0.0041	0.0054	0.0044	0.0047	0.0057	0.0047
{0, 2, 2}	-0.0124	-0.0124	-0.0117	-0.0118	-0.0126	-0.0113	-0.0113	-0.0141	-0.0111
{0, 2, 1}	0.0156	0.0150	0.0155	0.0149	0.0156	0.0151	0.0166	0.0132	0.0154
{0, 2, 4}	-0.0093	-0.0092	-0.0080	-0.0079	-0.0075	-0.0084	-0.0084	-0.0083	-0.0080
{0, 2, 7}	0.0098	0.0094	0.0071	0.0074	0.0067	0.0066	0.0067	0.0069	0.0062
{0, 2, 10}	-0.0125	-0.0113	-0.0093	-0.0093	-0.0084	-0.0091	-0.0078	-0.0072	-0.0066

di16:1PC (SLS),  $RH = 18 - 31\%$

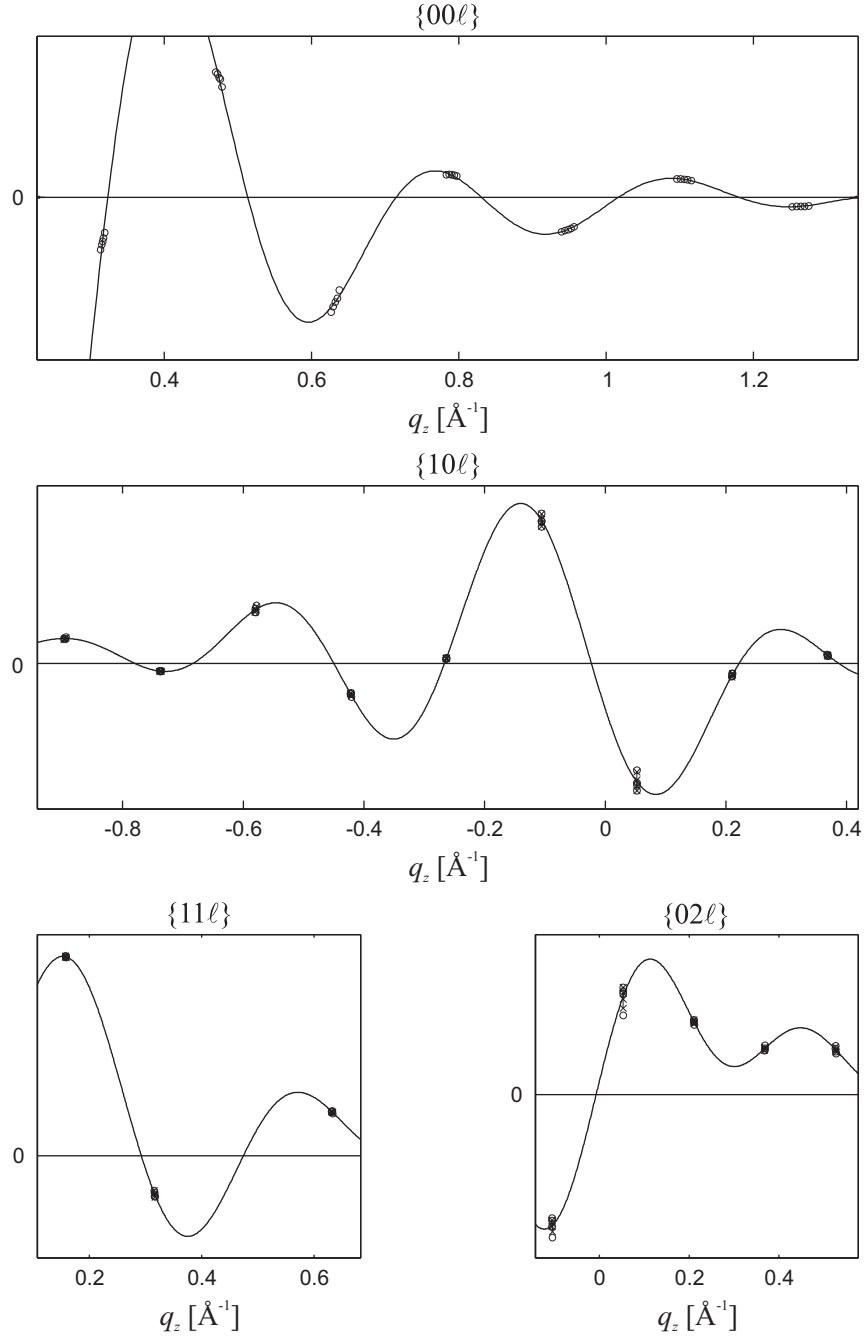




**di16:1PC (SLS),  $RH = 18 - 31\%$**

$RH$	18	22	25	28	31
$d$	41.93	42.14	42.38	42.56	42.88
$\sigma(d)$	0.07	0.10	0.06	0.10	0.05
$a$	61.85	62.93	63.86	65.37	67.10
$\sigma(a)$	0.20	0.01	0.16	0.17	0.07
$\{0, 0, 3\}$	-0.6302	-0.6791	-0.6943	-0.6662	-0.7171
$\{0, 0, 6\}$	0.0172	0.0149	0.0108	0.0073	0.0021
$\{0, 0, 9\}$	0.0665	0.0734	0.0771	0.0754	0.0839
$\{0, 0, 12\}$	-0.0573	-0.0650	-0.0703	-0.0702	-0.0806
$\{0, 0, 15\}$	0.0149	0.0163	0.0170	0.0165	0.0182
$\{0, 0, 18\}$	-0.0130	-0.0145	-0.0154	-0.0152	-0.0171
$\{0, 0, 21\}$	0.0084	0.0092	0.0095	0.0093	0.0102
$\{0, 0, 24\}^*$	0.0039	0.0043	0.0046	0.0045	0.0050
$\{1, 0, 20\}^*$	0.0152	0.0125	0.0094	0.0135	0.0096
$\{1, 0, 17\}$	-0.0217	-0.0185	-0.0167	-0.0228	-0.0168
$\{1, 0, 14\}$	0.0120	0.0110	0.0102	0.0118	0.0108
$\{1, 0, 11\}$	-0.0639	-0.0587	-0.0591	-0.0626	-0.0598
$\{1, 0, 8\}$	0.0326	0.0309	0.0274	0.0322	0.0313
$\{1, 0, 5\}$	0.0097	0.0056	0.0047	0.0048	0.0025
$\{1, 0, 2\}$	-0.1696	-0.1354	-0.1465	-0.1571	-0.1352
$\{1, 0, 1\}$	0.1193	0.1220	0.1169	0.1068	0.1045
$\{1, 0, 4\}^*$	0.0073	0.0055	0.0077	0.0097	0.0126
$\{1, 0, 7\}$	-0.0090	-0.0057	-0.0076	-0.0076	-0.0071
$\{1, 0, 13\}^*$	-0.0042	-0.0030	-0.0032	-0.0050	-0.0045
$\{1, 0, 16\}^*$	-0.0043	-0.0019	-0.0014	-0.0029	-0.0022
$\{1, 1, 0\}$	-0.0278	-0.0286	-0.0277	-0.0255	-0.0253
$\{1, 1, 3\}$	0.0335	0.0302	0.0312	0.0316	0.0293
$\{1, 1, 6\}$	-0.0113	-0.0079	-0.0076	-0.0079	-0.0050
$\{1, 1, 9\}$	0.0038	0.0016	0.0011	0.0000	0.0000
$\{1, 1, 12\}$	0.0062	0.0060	0.0052	0.0073	0.0051
$\{0, 2, 5\}^*$	0.0057	0.0041	0.0040	0.0036	0.0035
$\{0, 2, 2\}$	-0.0168	-0.0162	-0.0166	-0.0146	-0.0194
$\{0, 2, 1\}$	0.0188	0.0180	0.0198	0.0216	0.0176
$\{0, 2, 4\}$	-0.0130	-0.0094	-0.0103	-0.0117	-0.0065
$\{0, 2, 7\}$	0.0103	0.0089	0.0070	0.0076	0.0041
$\{0, 2, 10\}$	-0.0126	-0.0094	-0.0074	-0.0074	-0.0041

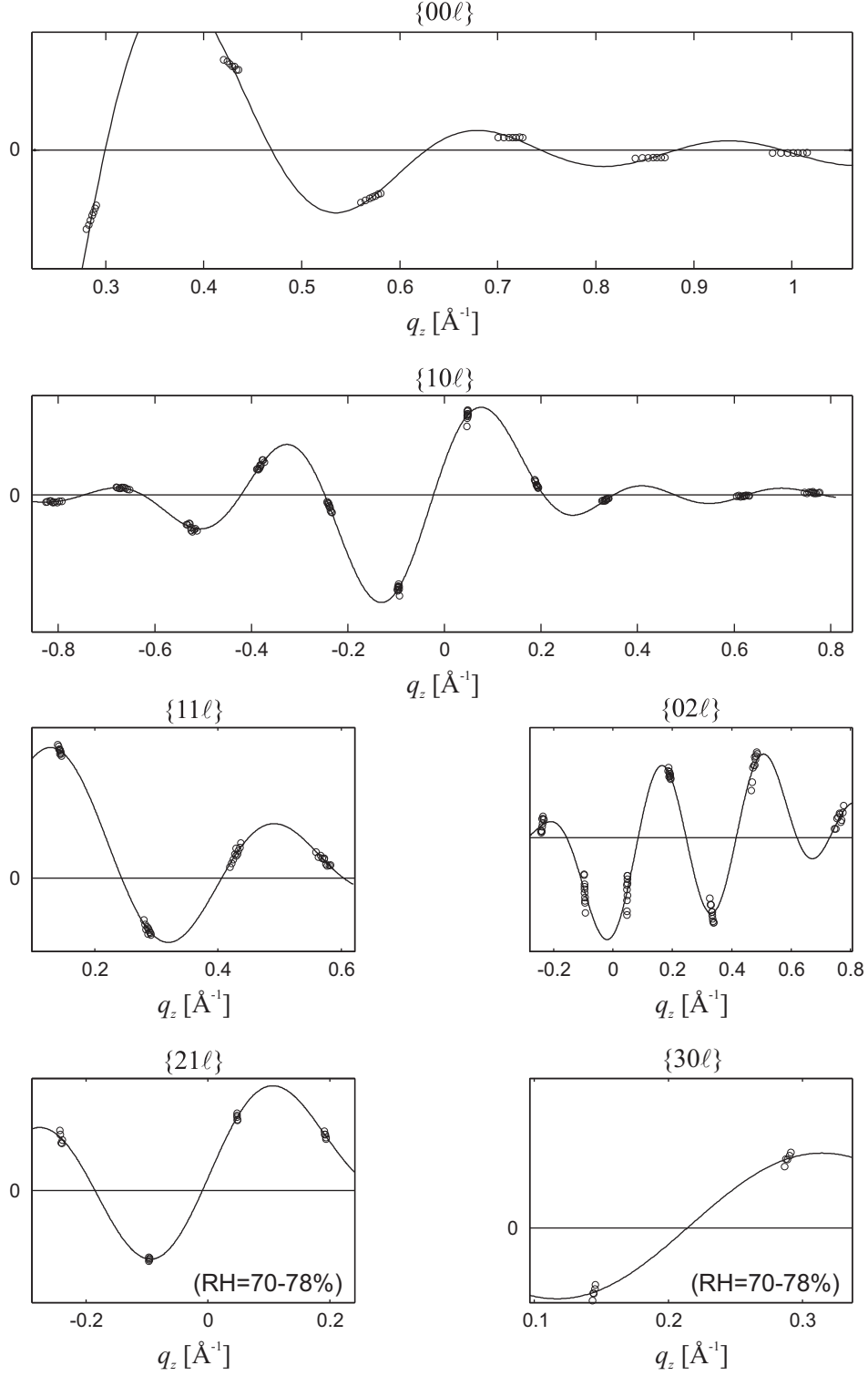
**di14:1PC (SLS),  $RH = 13.6 - 17\%$**



**di14:1PC (SLS),  $RH = 13.6 - 17\%$**

$RH$	13.6	14	15.6	17
$d$	39.68	39.72	39.77	39.85
$\sigma(d)$	0.07	0.06	0.11	0.17
$a$	60.87	61.14	61.96	62.93
$\sigma(a)$	0.01	0.29	0.24	0.01
$\{0, 0, 3\}$	-0.7611	-0.7523	-0.7644	-0.7466
$\{0, 0, 6\}$	-0.0301	-0.0304	-0.0317	-0.0321
$\{0, 0, 9\}$	0.0838	0.0834	0.0854	0.0844
$\{0, 0, 12\}$	-0.0729	-0.0729	-0.0751	-0.0748
$\{0, 0, 15\}$	0.0157	0.0156	0.0158	0.0155
$\{0, 0, 18\}$	-0.0226	-0.0225	-0.0231	-0.0229
$\{0, 0, 21\}$	0.0125	0.0124	0.0127	0.0125
$\{0, 0, 24\}^*$	-0.0065	-0.0064	-0.0066	-0.0065
$\{1, 0, \bar{17}\}$	-0.0197	-0.0210	-0.0204	-0.0232
$\{1, 0, \bar{14}\}$	0.0062	0.0065	0.0070	0.0066
$\{1, 0, \bar{11}\}$	-0.0422	-0.0465	-0.0420	-0.0511
$\{1, 0, \bar{8}\}$	0.0251	0.0258	0.0243	0.0298
$\{1, 0, \bar{5}\}$	-0.0036	-0.0041	-0.0046	-0.0045
$\{1, 0, \bar{2}\}$	-0.1119	-0.1207	-0.1173	-0.1322
$\{1, 0, 1\}$	0.1045	0.1011	0.1001	0.0941
$\{1, 0, 4\}$	0.0084	0.0083	0.0106	0.0118
$\{1, 0, 7\}$	-0.0060	-0.0065	-0.0071	-0.0079
$\{1, 1, 0\}$	-0.0254	-0.0249	-0.0250	-0.0240
$\{1, 1, 3\}$	0.0213	0.0220	0.0215	0.0230
$\{1, 1, 6\}$	-0.0044	-0.0045	-0.0040	-0.0040
$\{1, 1, 12\}$	0.0045	0.0049	0.0047	0.0051
$\{0, 2, \bar{2}\}$	-0.0143	-0.0141	-0.0135	-0.0167
$\{0, 2, 1\}$	0.0109	0.0116	0.0116	0.0092
$\{0, 2, 4\}$	-0.0075	-0.0082	-0.0079	-0.0087
$\{0, 2, 7\}$	0.0050	0.0055	0.0048	0.0052
$\{0, 2, 10\}$	-0.0044	-0.0048	-0.0053	-0.0053

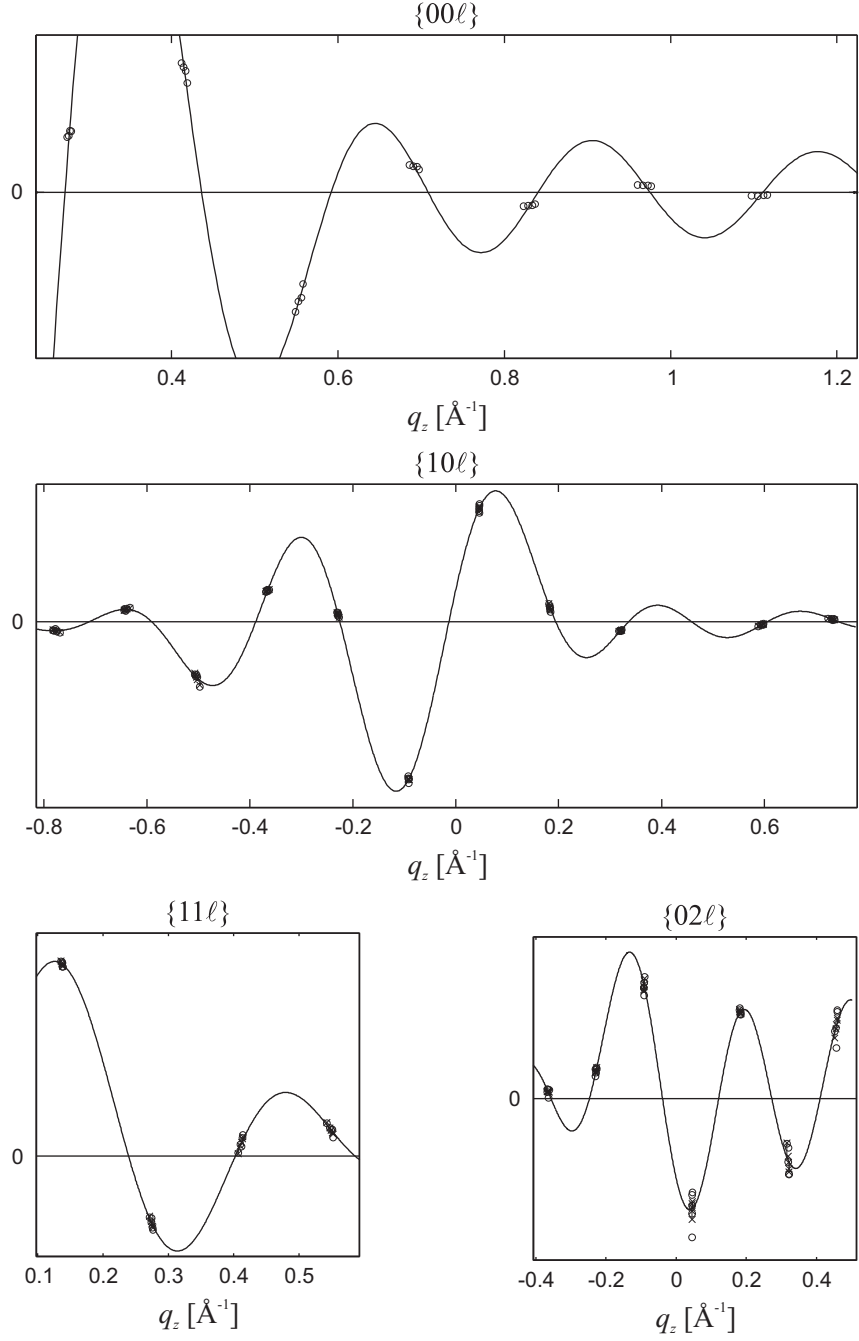
DPhPC (SLS),  $RH = 62 - 78\%$



DPhPC (SLS),  $RH = 62 - 78\%$

$RH$	62	64	66	68	70	70	72	74	76	78
$d$	43.15	43.27	43.54	43.69	43.87	43.92	44.13	44.38	44.63	44.94
$\sigma(d)$	0.10	0.06	0.16	0.09	0.09	0.16	0.07	0.16	0.01	0.11
$a$	60.73	61.34	61.54	62.21	62.93	63.09	63.92	64.86	65.92	67.71
$\sigma(a)$	0.23	0.01	0.29	0.13	0.01	0.07	0.07	0.08	0.20	0.15
<hr/>										
$\{0, 0, 3\}$	-0.6130	-0.6133	-0.6598	-0.6705	-0.6615	-0.6499	-0.6696	-0.6729	-0.6922	-0.6818
$\{0, 0, 6\}$	-0.0457	-0.0471	-0.0545	-0.0575	-0.0591	-0.0588	-0.0635	-0.0673	-0.0728	-0.0760
$\{0, 0, 9\}$	0.0673	0.0680	0.0747	0.0768	0.0768	0.0758	0.0793	0.0812	0.0850	0.0856
$\{0, 0, 12\}$	-0.0361	-0.0366	-0.0408	-0.0423	-0.0426	-0.0421	-0.0444	-0.0459	-0.0485	-0.0494
$\{0, 0, 15\}$	0.0109	0.0109	0.0116	0.0118	0.0116	0.0114	0.0117	0.0117	0.0119	0.0117
$\{0, 0, 18\}$	-0.0062	-0.0062	-0.0068	-0.0070	-0.0070	-0.0069	-0.0072	-0.0073	-0.0076	-0.0076
$\{0, 0, 21\}^*$	-0.0023	-0.0023	-0.0025	-0.0025	-0.0025	-0.0025	-0.0025	-0.0026	-0.0027	-0.0026
$\{1, 0, 20\}^*$	0.0046	0.0030	0.0013	0.0014	0.0038	-0.0272	-0.0288	-0.0298	-0.0316	-0.0322
$\{1, 0, 17\}$	-0.0132	-0.0121	-0.0101	-0.0105	-0.0124	-0.0130	-0.0118	-0.0127	-0.0110	-0.0112
$\{1, 0, 14\}$	0.0130	0.0124	0.0105	0.0103	0.0120	0.0120	0.0113	0.0110	0.0091	0.0087
$\{1, 0, 11\}$	-0.0519	-0.0524	-0.0479	-0.0486	-0.0548	-0.0583	-0.0587	-0.0565	-0.0557	-0.0620
$\{1, 0, 8\}$	0.0441	0.0453	0.0423	0.0441	0.0470	0.0485	0.0469	0.0558	0.0565	0.0563
$\{1, 0, 5\}$	-0.0123	-0.0143	-0.0142	-0.0159	-0.0188	-0.0189	-0.0205	-0.0256	-0.0282	-0.0305
$\{1, 0, 2\}$	-0.1643	-0.1683	-0.1557	-0.1532	-0.1560	-0.1496	-0.1418	-0.1483	-0.1545	-0.1742
$\{1, 0, 1\}$	0.1391	0.1370	0.1419	0.1410	0.1356	0.1322	0.1320	0.1276	0.1259	0.1177
$\{1, 0, 4\}$	0.0125	0.0119	0.0132	0.0148	0.0171	0.0150	0.0162	0.0209	0.0232	0.0258
$\{1, 0, 7\}$	-0.0067	-0.0065	-0.0071	-0.0072	-0.0079	-0.0091	-0.0090	-0.0097	-0.0096	-0.0108
$\{1, 0, 13\}^*$	-0.0021	-0.0012	-0.0016	-0.0012	-0.0023	-0.0026	-0.0025	-0.0029	-0.0015	-0.0030
$\{1, 0, 16\}^*$	0.0039	0.0027	0.0024	0.0021	0.0032	0.0048	0.0040	0.0044	0.0024	0.0034
$\{1, 1, 0\}$	-0.0232	-0.0236	-0.0263	-0.0273	-0.0275	-0.0272	-0.0288	-0.0298	-0.0316	-0.0322
$\{1, 1, 3\}$	0.0297	0.0305	0.0298	0.0299	0.0301	0.0285	0.0287	0.0292	0.0303	0.0323
$\{1, 1, 6\}$	-0.0140	-0.0136	-0.0128	-0.0122	-0.0119	-0.0129	-0.0110	-0.0117	-0.0108	-0.0102
$\{1, 1, 9\}$	0.0085	0.0074	0.0064	0.0056	0.0052	0.0068	0.0053	0.0041	0.0034	0.0026
$\{1, 1, 12\}$	0.0031	0.0031	0.0028	0.0032	0.0046	0.0043	0.0044	0.0050	0.0048	0.0062
$\{0, 2, 2\}$	-0.0079	-0.0079	-0.0096	-0.0106	-0.0114	-0.0123	-0.0128	-0.0121	-0.0140	-0.0140
$\{0, 2, 1\}$	0.0081	0.0082	0.0086	0.0094	0.0119	-0.0099	-0.0116	-0.0130	-0.0127	-0.0159
$\{0, 2, 4\}$	-0.0123	-0.0127	-0.0128	-0.0131	-0.0131	0.0156	0.0145	0.0134	0.0135	0.0129
$\{0, 2, 7\}$	0.0180	0.0183	0.0173	0.0166	0.0153	-0.0162	-0.0140	-0.0138	-0.0111	-0.0099
$\{0, 2, 10\}$	-0.0177	-0.0183	-0.0168	-0.0160	-0.0148	-0.0048	-0.0040	-0.0038	-0.0018	-0.0018
$\{0, 2, 13\}^*$	0.0043	0.0029	0.0017	0.0012	0.0026	0.0000	0.0000	0.0000	0.0000	0.0000
$\{0, 2, 16\}^*$	-0.0067	-0.0053	-0.0036	-0.0032	-0.0048	0.0000	0.0000	0.0000	0.0000	0.0000
$\{2, 1, 5\}^*$	-0.0044	-0.0042	-0.0034	-0.0034	-0.0036	—	—	—	—	—
$\{2, 1, 2\}^*$	0.0050	0.0053	0.0050	0.0049	0.0049	—	—	—	—	—
$\{2, 1, 1\}^*$	-0.0052	-0.0053	-0.0054	-0.0055	-0.0053	—	—	—	—	—
$\{2, 1, 4\}^*$	-0.0039	-0.0039	-0.0040	-0.0040	-0.0043	—	—	—	—	—
$\{3, 0, 3\}^*$	-0.0025	-0.0028	-0.0029	-0.0028	-0.0031	—	—	—	—	—
$\{3, 0, 6\}^*$	0.0034	0.0032	0.0029	0.0029	0.0026	—	—	—	—	—

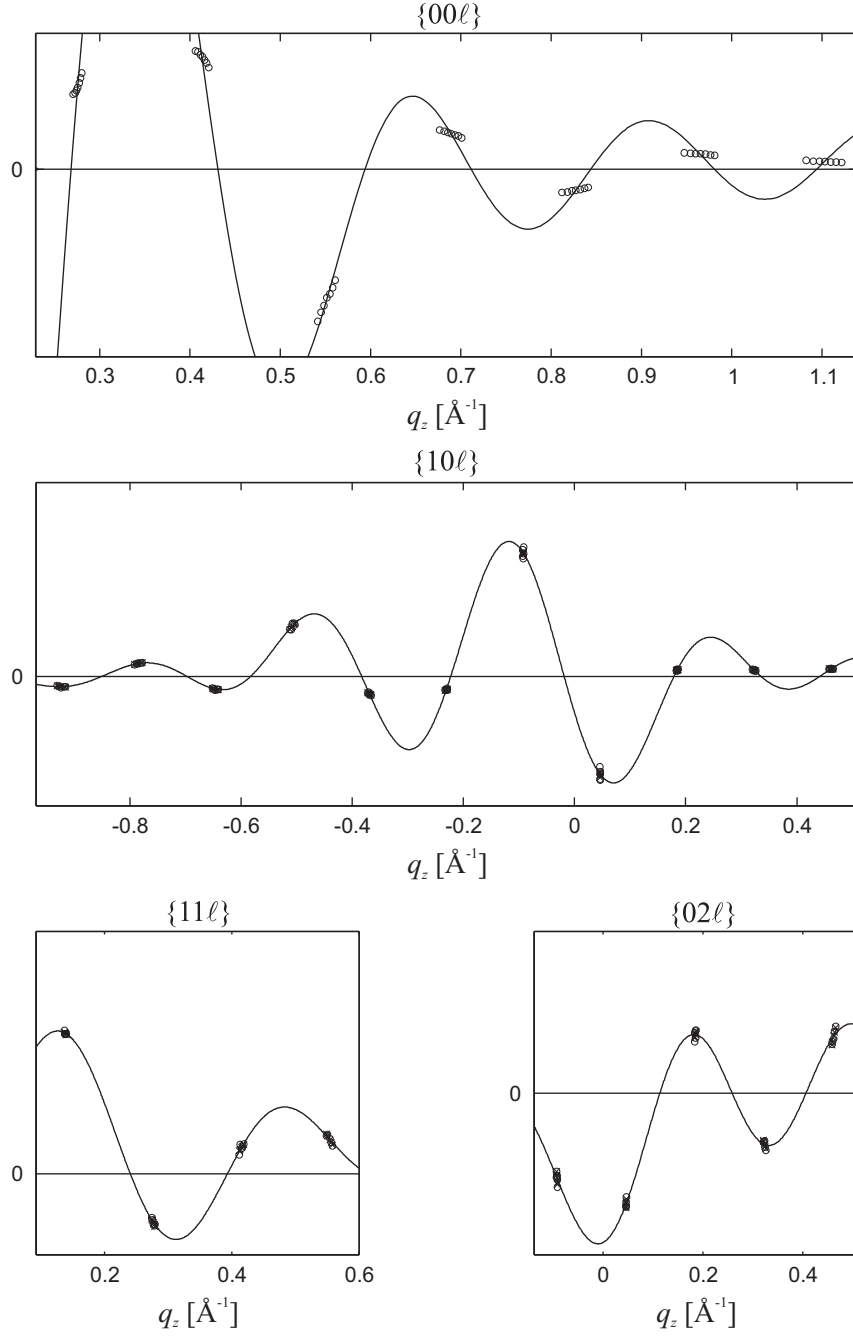
DOPC/DOPE 1:1 (SLS),  $RH = 68 - 74\%$



**DOPC/DOPE 1:1 (SLS),  $RH = 68 - 74\%$**

$RH$	68	70	72	72	74
$d$	45.50	45.59	45.77	45.93	46.31
$\sigma(d)$	0.08	0.01	0.32	0.12	0.20
$a$	68.43	69.65	72.11	71.19	73.56
$\sigma(a)$	0.08	0.16	0.39	0.31	0.02
<hr/>					
$\{0, 0, 3\}$	-0.7114	-0.7135	-0.7239	-0.7259	-0.7339
$\{0, 0, 6\}$	0.0289	0.0285	0.0281	0.0274	0.0259
$\{0, 0, 9\}$	0.0620	0.0632	0.0661	0.0682	0.0732
$\{0, 0, 12\}$	-0.0549	-0.0565	-0.0602	-0.0630	-0.0698
$\{0, 0, 15\}$	0.0131	0.0134	0.0140	0.0144	0.0155
$\{0, 0, 18\}$	-0.0066	-0.0067	-0.0071	-0.0073	-0.0079
$\{0, 0, 21\}$	0.0036	0.0037	0.0038	0.0040	0.0043
$\{0, 0, 24\}^*$	-0.0016	-0.0017	-0.0018	-0.0019	-0.0022
$\{1, 0, 17\}$	-0.0086	-0.0089	-0.0076	-0.0090	-0.0095
$\{1, 0, 14\}$	0.0109	0.0117	0.0104	0.0113	0.0117
$\{1, 0, 11\}$	-0.0520	-0.0522	-0.0528	-0.0509	-0.0559
$\{1, 0, 8\}$	0.0291	0.0284	0.0312	0.0286	0.0271
$\{1, 0, 5\}$	0.0089	0.0077	0.0057	0.0064	0.0034
$\{1, 0, 2\}$	-0.1542	-0.1467	-0.1609	-0.1445	-0.1340
$\{1, 0, 1\}$	0.1134	0.1111	0.1078	0.1034	0.0939
$\{1, 0, 4\}^*$	0.0095	0.0113	0.0154	0.0127	0.0149
$\{1, 0, 7\}$	-0.0081	-0.0087	-0.0096	-0.0087	-0.0084
$\{1, 0, 13\}^*$	-0.0022	-0.0033	-0.0029	-0.0033	-0.0042
$\{1, 0, 16\}^*$	0.0015	0.0023	0.0013	0.0022	0.0024
$\{1, 1, 0\}$	-0.0210	-0.0212	-0.0219	-0.0223	-0.0233
$\{1, 1, 3\}$	0.0294	0.0284	0.0305	0.0279	0.0263
$\{1, 1, 6\}$	-0.0115	-0.0108	-0.0098	-0.0097	-0.0083
$\{1, 1, 9\}$	0.0032	0.0027	0.0015	0.0016	0.0004
$\{1, 1, 12\}$	0.0029	0.0040	0.0041	0.0041	0.0044
$\{0, 2, 8\}^*$	-0.0008	-0.0011	-0.0011	-0.0001	-0.0009
$\{0, 2, 5\}^*$	-0.0028	-0.0035	-0.0033	-0.0036	-0.0032
$\{0, 2, 2\}$	-0.0139	-0.0133	-0.0131	-0.0135	-0.0132
$\{0, 2, 1\}$	0.0118	0.0117	0.0176	0.0125	0.0125
$\{0, 2, 4\}$	-0.0107	-0.0101	-0.0107	-0.0105	-0.0096
$\{0, 2, 7\}$	0.0095	0.0091	0.0063	0.0074	0.0050
$\{0, 2, 10\}$	-0.0111	-0.0105	-0.0064	-0.0082	-0.0073

di18:1PC/DOPC (ESRF),  $RH = 24 - 32\%$

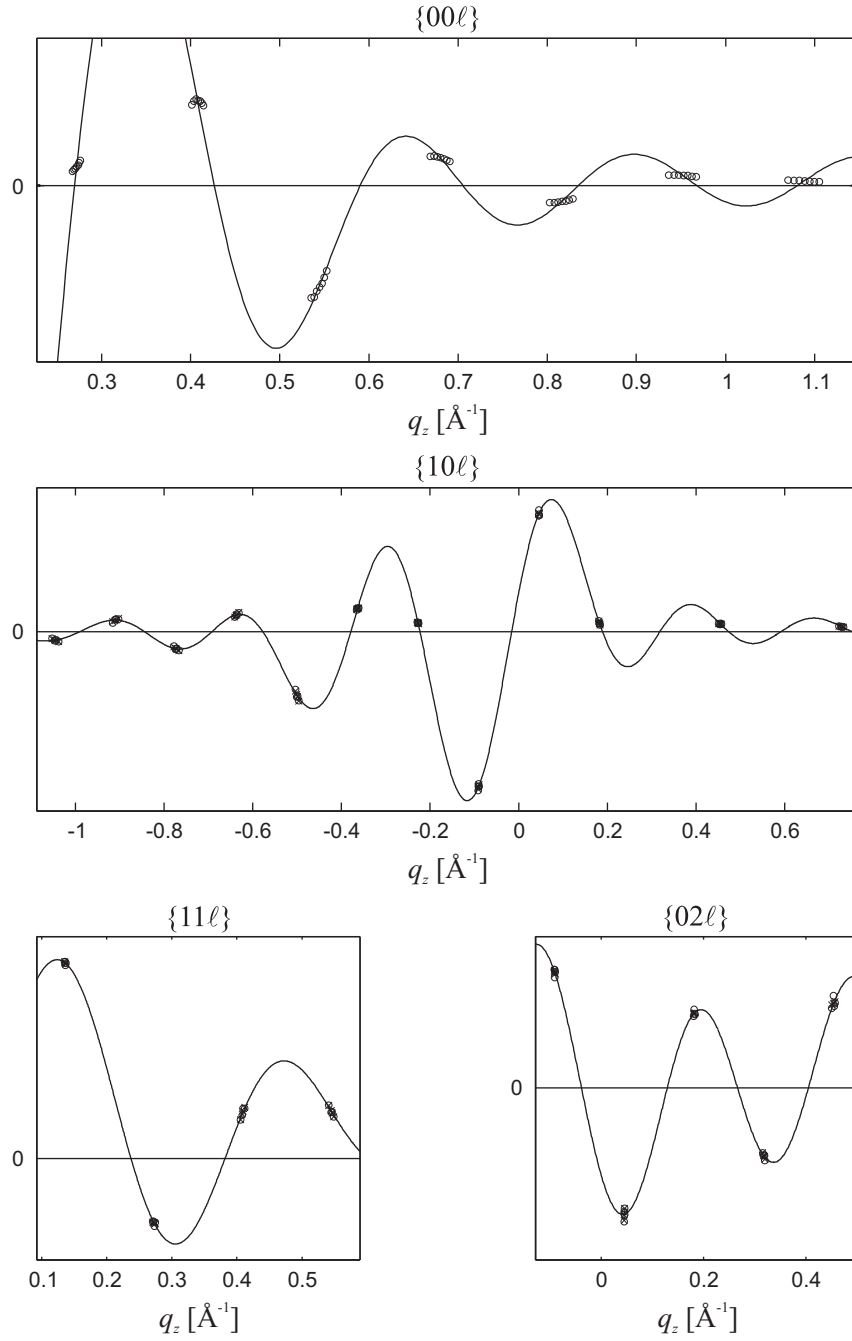




di18:1PC/DOPC (ESRF),  $RH = 24 - 32\%$

$RH$	24	26	28	30	32
$D$	44.99	45.18	45.34	45.62	45.75
$\sigma(d)$	0.22	0.23	0.25	0.27	0.25
$a$	64.01	65.13	65.69	66.50	67.41
$\sigma(a)$	0.41	0.46	0.68	0.36	0.44
$\{0, 0, 3\}$	-0.6014	-0.6376	-0.6298	-0.6352	-0.6292
$\{0, 0, 6\}$	0.0388	0.0399	0.0384	0.0369	0.0358
$\{0, 0, 9\}$	0.0446	0.0481	0.0482	0.0498	0.0498
$\{0, 0, 12\}$	-0.0493	-0.0543	-0.0554	-0.0588	-0.0595
$\{0, 0, 15\}$	0.0138	0.0150	0.0151	0.0158	0.0159
$\{0, 0, 18\}$	-0.0082	-0.0089	-0.0090	-0.0095	-0.0095
$\{0, 0, 21\}$	0.0059	0.0064	0.0064	0.0067	0.0067
$\{0, 0, 24\}^*$	0.0029	0.0032	0.0032	0.0034	0.0034
$\{1, 0, 20\}^*$	0.0115	0.0114	0.0124	0.0116	0.0117
$\{1, 0, 17\}$	-0.0142	-0.0139	-0.0145	-0.0141	-0.0154
$\{1, 0, 14\}$	0.0142	0.0145	0.0151	0.0144	0.0146
$\{1, 0, 11\}$	-0.0569	-0.0527	-0.0576	-0.0578	-0.0579
$\{1, 0, 8\}$	0.0205	0.0182	0.0195	0.0197	0.0219
$\{1, 0, 5\}$	0.0170	0.0154	0.0153	0.0146	0.0139
$\{1, 0, 2\}$	-0.1538	-0.1367	-0.1286	-0.1331	-0.1457
$\{1, 0, 1\}$	0.1162	0.1181	0.1125	0.1062	0.1020
$\{1, 0, 4\}^*$	-0.0086	-0.0073	-0.0059	-0.0073	-0.0064
$\{1, 0, 7\}$	-0.0066	-0.0062	-0.0065	-0.0072	-0.0076
$\{1, 0, 10\}^*$	-0.0091	-0.0080	-0.0083	-0.0078	-0.0083
$\{1, 1, 0\}$	-0.0280	-0.0288	-0.0277	-0.0266	-0.0258
$\{1, 1, 3\}$	0.0273	0.0254	0.0244	0.0243	0.0258
$\{1, 1, 6\}$	-0.0099	-0.0094	-0.0089	-0.0080	-0.0079
$\{1, 1, 9\}$	0.0057	0.0049	0.0044	0.0051	0.0034
$\{1, 1, 12\}$	0.0054	0.0057	0.0061	0.0068	0.0068
$\{0, 2, 2\}$	-0.0153	-0.0154	-0.0144	-0.0149	-0.0171
$\{0, 2, 1\}$	0.0203	0.0198	0.0199	0.0197	0.0203
$\{0, 2, 4\}$	-0.0122	-0.0100	-0.0108	-0.0105	-0.0092
$\{0, 2, 7\}$	0.0112	0.0099	0.0083	0.0085	0.0088
$\{0, 2, 10\}$	-0.0129	-0.0112	-0.0095	-0.0089	-0.0088

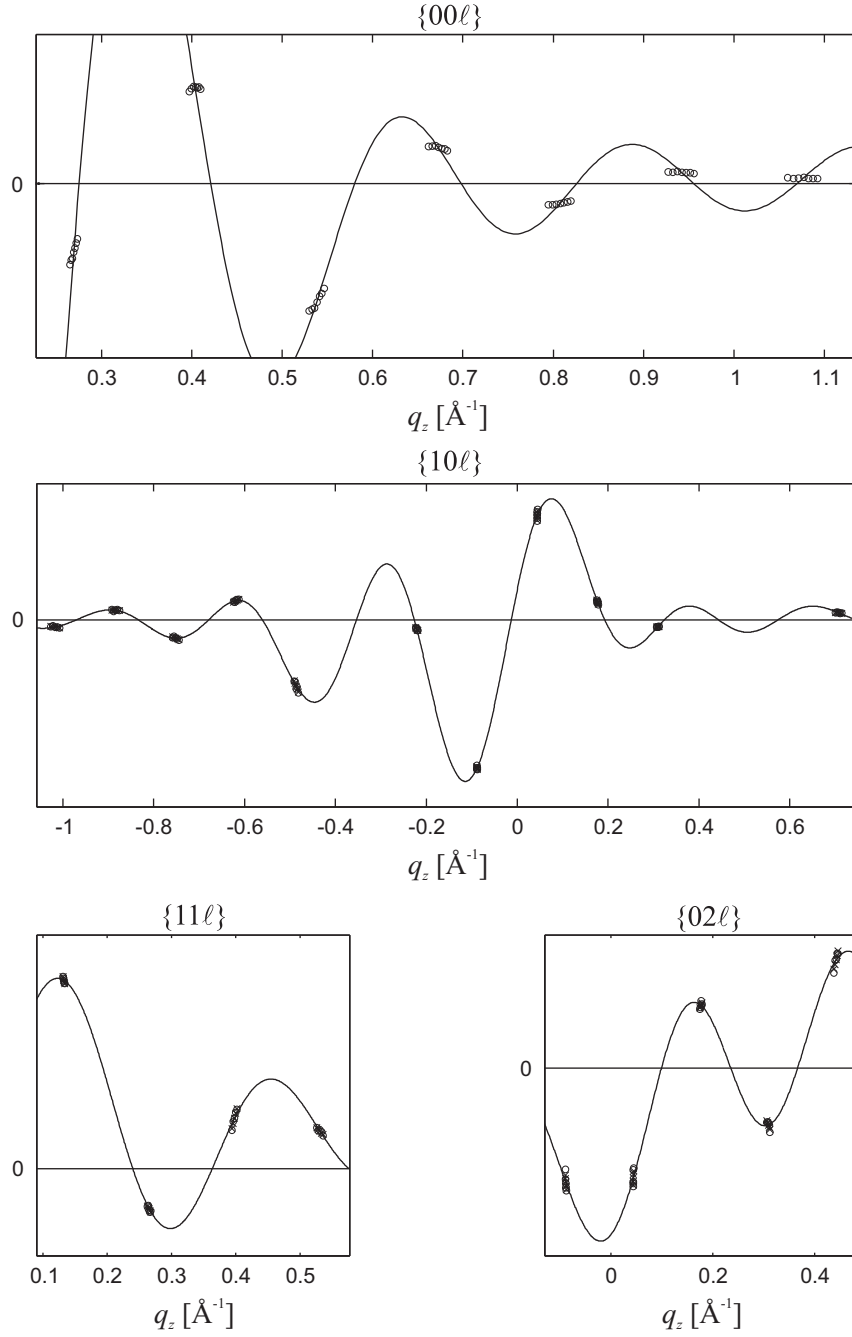
DOPC/Chol 90:10 (ESRF),  $RH = 36 - 42\%$



**DOPC/Chol 90:10 (ESRF),  $RH = 36 - 42\%$**

$RH$	36	38	40	42
$d$	45.79	46.01	46.15	46.45
$\sigma(d)$	0.29	0.28	0.36	0.30
$a$	66.38	67.81	68.02	69.10
$\sigma(a)$	0.51	0.44	0.75	0.73
$\{0, 0, 3\}$	-0.5790	-0.5863	-0.5970	-0.5983
$\{0, 0, 6\}$	0.0119	0.0112	0.0108	0.0096
$\{0, 0, 9\}$	0.0447	0.0453	0.0462	0.0463
$\{0, 0, 12\}$	-0.0504	-0.0531	-0.0554	-0.0584
$\{0, 0, 15\}$	0.0141	0.0147	0.0152	0.0157
$\{0, 0, 18\}$	-0.0079	-0.0083	-0.0086	-0.0090
$\{0, 0, 21\}$	0.0051	0.0053	0.0055	0.0057
$\{0, 0, 24\}^*$	0.0023	0.0024	0.0026	0.0027
$\{1, 0, \bar{2}3\}^*$	-0.0081	-0.0107	-0.0092	-0.0106
$\{1, 0, \bar{2}0\}^*$	0.0111	0.0145	0.0144	0.0139
$\{1, 0, \bar{1}7\}$	-0.0180	-0.0205	-0.0192	-0.0206
$\{1, 0, \bar{1}4\}$	0.0185	0.0190	0.0198	0.0210
$\{1, 0, \bar{1}1\}$	-0.0715	-0.0769	-0.0725	-0.0758
$\{1, 0, \bar{8}\}$	0.0271	0.0276	0.0263	0.0263
$\{1, 0, \bar{5}\}$	0.0120	0.0106	0.0096	0.0093
$\{1, 0, \bar{2}\}$	-0.1964	-0.1821	-0.1717	-0.1705
$\{1, 0, 1\}$	0.1438	0.1388	0.1371	0.1281
$\{1, 0, 4\}$	0.0085	0.0097	0.0094	0.0119
$\{1, 0, 10\}^*$	0.0095	0.0099	0.0084	0.0089
$\{1, 0, 16\}^*$	0.0061	0.0059	0.0059	0.0062
$\{1, 1, 0\}$	-0.0383	-0.0371	-0.0368	-0.0345
$\{1, 1, 3\}$	0.0311	0.0293	0.0286	0.0279
$\{1, 1, 6\}$	-0.0102	-0.0103	-0.0091	-0.0090
$\{1, 1, 9\}$	0.0079	0.0075	0.0062	0.0054
$\{1, 1, 12\}$	0.0066	0.0071	0.0067	0.0075
$\{0, 2, \bar{2}\}$	-0.0211	-0.0200	-0.0179	-0.0184
$\{0, 2, 1\}$	0.0216	0.0217	0.0203	0.0214
$\{0, 2, 4\}$	-0.0131	-0.0126	-0.0127	-0.0114
$\{0, 2, 7\}$	0.0130	0.0115	0.0111	0.0105
$\{0, 2, 10\}$	-0.0151	-0.0138	-0.0150	-0.0126

DOPC/Chol 70:30 (ESRF),  $RH = 50 - 60\%$



**DOPC/Chol 70:30 (ESRF),  $RH = 50 - 60\%$**

$RH$	50	52	54	56	58	60
$d$	46.75	46.94	47.14	47.36	47.60	47.82
$\sigma(d)$	0.32	0.32	0.29	0.28	0.32	0.33
$a$	69.06	70.06	70.76	71.62	72.54	74.44
$\sigma(a)$	0.45	0.42	0.76	0.82	0.57	0.41
<hr/>						
$\{0, 0, 3\}$	-0.6933	-0.7197	-0.7219	-0.6968	-0.7065	-0.6924
$\{0, 0, 6\}$	-0.0271	-0.0295	-0.0310	-0.0314	-0.0335	-0.0343
$\{0, 0, 9\}$	0.0369	0.0381	0.0380	0.0365	0.0368	0.0358
$\{0, 0, 12\}$	-0.0461	-0.0490	-0.0504	-0.0499	-0.0520	-0.0523
$\{0, 0, 15\}$	0.0139	0.0147	0.0150	0.0147	0.0152	0.0151
$\{0, 0, 18\}$	-0.0078	-0.0083	-0.0085	-0.0084	-0.0088	-0.0089
$\{0, 0, 21\}$	0.0043	0.0045	0.0046	0.0045	0.0047	0.0047
$\{0, 0, 24\}^*$	0.0020	0.0021	0.0022	0.0021	0.0022	0.0022
$\{1, 0, \bar{20}\}^*$	0.0095	0.0090	0.0076	0.0084	0.0081	0.0074
$\{1, 0, \bar{17}\}$	-0.0162	-0.0162	-0.0150	-0.0162	-0.0159	-0.0168
$\{1, 0, \bar{14}\}$	0.0178	0.0162	0.0156	0.0171	0.0163	0.0166
$\{1, 0, \bar{11}\}$	-0.0622	-0.0558	-0.0554	-0.0608	-0.0555	-0.0601
$\{1, 0, \bar{8}\}$	0.0165	0.0153	0.0155	0.0162	0.0143	0.0152
$\{1, 0, \bar{5}\}$	-0.0072	-0.0072	-0.0077	-0.0082	-0.0089	-0.0088
$\{1, 0, \bar{2}\}$	-0.1454	-0.1320	-0.1327	-0.1315	-0.1225	-0.1232
$\{1, 0, 1\}$	0.0991	0.0996	0.0964	0.0893	0.0865	0.0810
$\{1, 0, 4\}$	0.0127	0.0136	0.0149	0.0162	0.0146	0.0159
$\{1, 0, 7\}$	-0.0073	-0.0064	-0.0059	-0.0065	-0.0057	-0.0062
$\{1, 1, 0\}$	-0.0244	-0.0231	-0.0207	-0.0173	-0.0146	-0.0116
$\{1, 1, 3\}$	0.0248	0.0235	0.0233	0.0232	0.0220	0.0221
$\{1, 1, 6\}$	-0.0065	-0.0054	-0.0055	-0.0051	-0.0043	-0.0044
$\{1, 1, 9\}$	0.0082	0.0075	0.0070	0.0062	0.0054	0.0044
$\{1, 1, 12\}$	0.0047	0.0042	0.0046	0.0048	0.0044	0.0047
$\{0, 2, \bar{2}\}$	-0.0156	-0.0163	-0.0147	-0.0171	-0.0154	-0.0164
$\{0, 2, 1\}$	0.0165	0.0147	0.0167	0.0146	0.0152	0.0158
$\{0, 2, 4\}$	-0.0096	-0.0093	-0.0090	-0.0095	-0.0080	-0.0078
$\{0, 2, 7\}$	0.0100	0.0095	0.0084	0.0079	0.0073	0.0073
$\{0, 2, 10\}$	-0.0190	-0.0167	-0.0165	-0.0155	-0.0143	-0.0126